AFM Bi-material Cantilever Based Near-field Radiation Heat Transfer Measurement

by

Ramteja Reddy Kondakindi

A Thesis Presented in Partial Fulfillment
of the Requirements for the Degree
Master of Science

Approved June 2019 by the
Graduate Supervisory Committee:

Liping Wang, Chair
Beomjin Kwon
Qing Hua Wang

ARIZONA STATE UNIVERSITY

August 2019

ABSTRACT

Near-field thermal radiation occurs when the distance between two surfaces at different temperatures is less than the characteristic wavelength of thermal radiation. While theoretical studies predict that the near-field radiative heat transfer could exceed Planck's blackbody limit in the far-field by orders of magnitudes depending on the materials and gap distance, experimental measurement of super-Planckian near-field radiative heat flux is extremely challenging in particular at sub-100-nm vacuum gaps and few has been demonstrated. The objective of this thesis is to develop a novel thermal metrology based on AFM bi-material cantilever and experimentally measure near-field thermal radiation.

The experiment setup is completed and validated by measuring the near-field radiative heat transfer between a silica microsphere and a silica substrate and comparing with theoretical calculations. The bi-material AFM cantilever made of SiNi and Au bends with temperature changes, whose deflection is monitored by the position-sensitive diode. After careful calibration, the bi-material cantilever works as a thermal sensor, from which the near-field radiative conductance and tip temperature can be deduced when the silica substrate approaches the silica sphere attached to the cantilever by a piezo stage with a resolution of 1 nm from a few micrometers away till physical contact. The developed novel near-field thermal metrology will be used to measure the near-field radiative heat transfer between the silica microsphere and planar SiC surface as well as nanostructured SiC metasurface. This research aims to enhance the fundamental understandings of radiative heat transfer in the near-field which could lead to advances in microelectronics, optical data storage and thermal systems for energy conversion and thermal management.

i

ACKNOWLEDGMENTS

I would like to thank my thesis chair Dr. Liping Wang for giving me an opportunity to work under his supervision and carry out this research. I would like to thank my committee members Dr. Beomjin Kwon and Dr. Qing Hua Wang for their time, support and guidance while reviewing this thesis. I would also like to thank Dr. Jui-Yung Chang and all other members of the Nano-Engineered Thermal Radiation research group for their support and help during the thesis. I am also grateful to all my friends and family who supported me during the period I was working on this thesis.

TABLE OF CONTENTS

iii

LIST OF TABLES

LIST OF FIGURES

CHAPTER 1 BACKGROUND AND LITERATURE REVIEW

1.1 Far-Field and Near-Field Thermal Radiation

A blackbody is considered to be a perfect emitter and absorber of thermal radiation in the far-field. At a specified temperature and wavelength, no surface can emit more energy than a blackbody. The expression for spectral blackbody emissive power is developed by Planck which is [1]

$$E_{b\lambda}(T,\lambda) = \frac{C_1}{n^2\lambda^5[e^{\frac{C_2}{n\lambda T}}-1]} \quad [\text{W} \cdot \text{m}^{-2} \cdot \text{µm}^{-1}] \tag{1.1}$$

$$C_1 = 2\pi h C_0^2 = 3.7418 \times 10^{-16} \quad [\text{W} \cdot \text{m}^{-2}] \tag{1.2}$$

$$C_2 = \frac{hC_0}{k} = 14{,}388 \quad [\text{µm} \cdot \text{K}] \tag{1.3}$$

where k_B is the Boltzmann's constant, T is the absolute temperature of the surface in Kelvin, λ is the wavelength of the radiation emitted in µm and n is the refractive index of the medium which is assumed to be constant.

From the integration of the spectral blackbody emissive power $E_{b\lambda}$ over the entire wavelength spectrum it gives the total blackbody emissive power E_b as

$$E_b(T) = \int_0^\infty E_{b\lambda}(T,\lambda)d\lambda = \sigma T^4 \quad [\text{W} \cdot \text{m}^{-2}] \tag{1.4}$$

where σ is the Stefan – Boltzmann constant.

Wien's displacement law states that the peak wavelength where spectral blackbody emissive power is maximum is inversely proportional to the temperature as

$$(n\lambda T)_{max} = 2898 \quad [\text{µm} \cdot \text{K}] \tag{1.5}$$

Planck's theory of blackbody radiation imposes a limit on the maximum radiative transfer between two objects at a given temperature difference. But recent research and experiments [2, 3] have proved that when two surfaces are close enough the near-field

1

radiation effects the radiative heat transfer and enhances the emissive power beyond the Planck's limit.
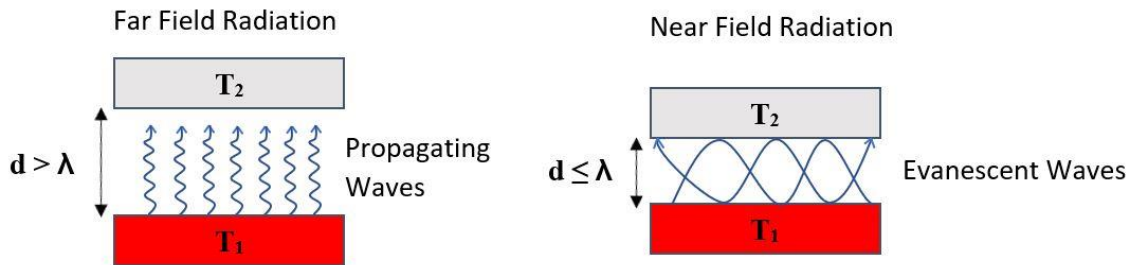
Figure 1.1: Schematic of Far-Field and Near-Field Radiation

When two surfaces are placed very close such that the distance between them is less than the characteristic wavelength of the radiation then the radiation is considered as near-field radiation (NFR). The coupling of evanescent waves or surface waves enhance the near-field radiation by a few orders of magnitude larger than the blackbody limit. Fig. 1.1 shows the schematic representation of far-field and near-field radiation. The propagating waves are dominating in far-field radiation as the evanescent waves decay as the gap between the surfaces is greater than the characteristic wavelength of the thermal radiation. During near-field radiation the evanescent waves dominate the propagating waves and increase the thermal radiation drastically.

When electromagnetic waves interact with the oscillatory movement of charges near the surface of plasmonic or phononic materials, it creates surface plasmon/phonon polaritons which enhances the local density of states within the nanometer vacuum gaps. The theoretical calculations of near-field radiation are based on fluctuational electrodynamics. At any finite temperature above absolute zero, chaotic thermal motions

take place inside any material. The charged particles of opposite sign pair up and create dipoles. The random motion of the dipoles induces fluctuating thermal currents and radiative heat transfer.

Fig. 1.2 shows the theoretical calculation of near-field heat flux between two plates separated with a gap d which varies from 10 nm to 10 μm. The plates materials used are silica and silicon carbide. From the calculations it is clear the near-field radiation is drastically increasing as the gap decreases and approaching the vacuum gaps in comparison to blackbody radiation limit.
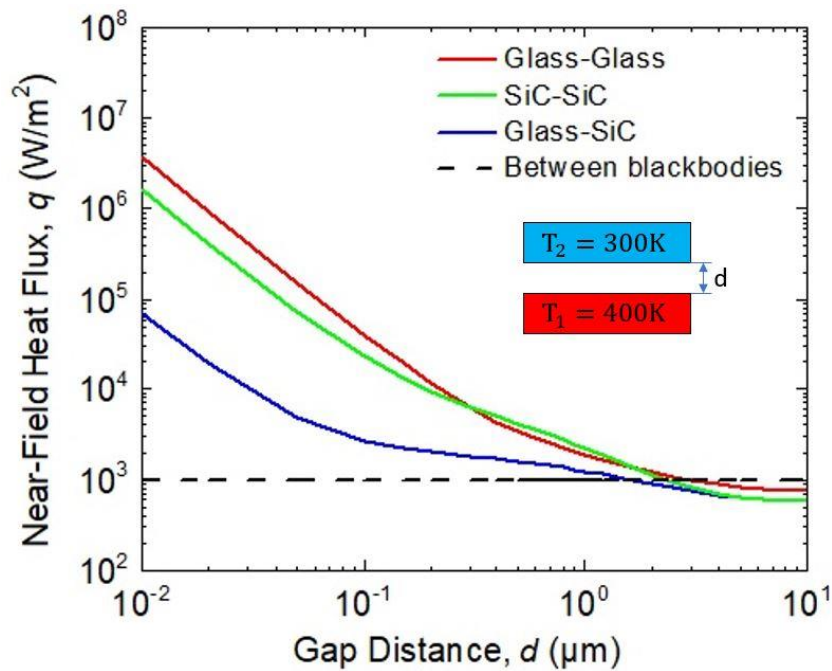
Figure 1.2: Theoretical Calculation of Near-Field Heat Flux vs. Gap between Plates

Near-field radiation has promising applications in energy conversion systems like thermophotovoltaic (TPV) where the efficiency can be increased as Basu et al [4] mentioned. The near-field radiation can be used for near-field imaging which is not restricted by the diffraction limit [5, 6]. Also, near-field radiation can be used as thermal

rectifier [7, 8]. Even nanolithography techniques based on surface plasmon waves are used for structure pattering of characteristic length less than 50 nm [9, 10].

1.2 Earlier Work on Near-Field Radiation Measurements

The Planck theory of blackbody radiation lays down the upper limit on the radiation heat transfer between two surfaces at the given temperatures. However, Planck's theory has been challenged in recent decades by theoretical predictions and experiments of the radiative heat transfer between two surfaces separated by nanoscale gaps which exceeds the Planck's limit significantly, in particular, when the two surfaces support surface polaritons.

Planck's theory [11] is not applicable when the characteristic dimensions of the objects are small or equal to the wavelength of the thermal radiation. Using fluctuational thermodynamics which was introduced by Rytov [12] the theory for near field thermal radiation is introduced by Polder and Van Hove [13]. In the last century there are only few experimental results showing the near-field radiation. Increased near-field radiative heat transfer between two metallic parallel plates at gaps of 50 μm to 1 mm at cryogenic temperatures is reported by Domoto et al [14]. But the value is only 1/29 of Planck's theory calculations. Measurement of near-field radiation between two chromium plates by Hargreaves [15] yielded a value of 2.95 $W \cdot m^{-2} \cdot K^{-1}$ when compared to the far-field value of 1.75 $W \cdot m^{-2} \cdot K^{-1}$. Nonetheless the near-field radiation heat transfer is 50% less than the blackbody radiation heat transfer. Xu et al [16] could not detect any near-field radiation heat transfer due to low sensitivity of the experimental technique. Due to the few experimental results of near-field radiation and even fewer results of near-field radiation heat transfer exceeding blackbody radiation more precise measurements are required.

1.3 Recent Near-Field Radiation Measurement Techniques

Recently three main geometrical configurations have been used to measure the near-field thermal radiation: plate-plate, tip-plate, and sphere-plate configurations. The major challenges for NFR measurement in plate-plate configuration involve sample bow, parallelism, and dust particles that prevent the creation of nanometer gap distance across large lateral dimension without contacts between two planar surfaces. These drawbacks make it difficult for the measurements with gaps below 200 nm. In the tip-plate configuration the sample surface can be brought within a few nanometers close to the tip usually made of thermal scanning probes for measuring the near-field radiation. The main drawback for the tip-plate configuration is the limitation of tip materials which are usually metals for thermocouple to measure the tip temperature. The sphere-plate configuration is a compromise between the plate-plate and tip-plate in terms of challenges. Using sphere-plate configuration the near-field radiation heat transfer can be measured below 200 nm gaps without the challenges faced in plate-plate configuration with different materials for the sphere attached to an AFM cantilever. In this way, polar materials like silica which support surface phonon polaritons can be used for observing strong near-field effects.

Arvind Narayanaswamy et al [17] measured the near-field radiative heat transfer between two glass surfaces at a gap of 1.6 μm. The gap is maintained by using the polystyrene microspheres by placing them selectively on the glass surfaces. The dyadic Green's function technique [18] and the fluctuation dissipation theorem [19 - 21] are used to determine the near-field radiation heat transfer between two parallel glass surfaces. The measured heat transfer coefficient is 50% higher than Planck's blackbody radiation limit which is same as the theoretical calculations. Watjen et al [22] measured near-field

radiation heat transfer near room temperature between two doped-Si parallel plates with 1 cm^2 surface area from 200 nm to 780 nm gap. The measured radiative heat flux is 11 times as high as the blackbody limit for the same hot and cold surface temperatures. Experimental measurements of near-field radiative heat transfer between two parallel plates have hurdles that make it difficult to measure at gap below 1 μm. Plate-plate configuration have hurdles like maintaining and measuring the gap between the plates, maintaining the parallelism between the plates at nanoscale gaps, having good surface cleanliness (surface roughness), the deviation of the sphere diameter preventing the plates from being parallel to each other and also the gaps that can be used are restricted by the polystyrene available diameters. All these obstacles make it difficult to measure surface phonon polaritons enhanced heat transfer between dielectric materials.

Technological advancements in 21st century helped near-field radiation measurements at nanoscale gaps like using scanning tunneling microscope (STM) in a tip-plate configuration. Kittel et al [23] used STM and determined saturation of heat transfer at 10 nm gap which was caused by spatial dispersion effects. Kim et al [24] custom fabricated scanning probes with embedded thermocouples to measure radiative heat transfer at gaps as small as 2 nm. Selective metals and dielectric materials were deposited on the scanning probes to study the extreme near-field radiation between SiO_2-SiO_2, SiN-SiN and Au-Au surfaces. The results indicate that the SiO_2 near-field radiation is dominated by surface phonon polaritons and the heat transfer decreases as the gap size increases. Also, the Au-Au tip and substrate results suggest the heat transfer decreases slowly with increase in gap size. Cui et al [25] measured near-field radiative heat transfer between Au coated probe with embed thermocouples and heated Au substrate from few Å

6

to 5 nm gap in ultra-high vacuum. The results showed that systematic cleaning of the Au probe and substrate attenuated the deviations from predictions of fluctuational thermodynamics previously reported by Kittel et al [23]. Also, the deviations in sub nanometer gap are smaller in magnitude than reported by Kittel et al [23] which are attributed to monolayer level contaminations that are still present on the surfaces and cannot be detected by their probes.

A bi-material cantilever bends when there is a temperature change due to the different thermal expansion coefficients of the cantilever materials. The cantilevers are sensitive enough to detect a temperature in the range of 10^{-4} to 10^{-5} K and a power of 5×10^{-10} W [19], so they have been used as sensitive calorimeters [26, 27] and IR detectors [28, 29, 30]. Narayanaswamy et al [31] determined numerically the near-field radiative heat transfer between two spheres which helps in estimating the thermal conductance between a sphere and substrate. Using this theory, the thermal conductance between two spheres of 50 μm in diameter was predicted to be in the range of 10^{-9} to 10^{-8} W·K^{-1} for gaps from 100 nm to 10 μm. The conductance is in the range of sensitivity of the bi-material cantilevers.

Using Mie theory [32] the emissivity of the silica sphere with diameter of 50 μm is determined to be 0.97. The emissivity value makes the far-field radiation between the sphere and substrate approximately equal to blackbody radiation. The maximum measured conductance due to near-field is 6 nW·K^{-1} above the Planck's theory of blackbody radiation value of 29 nW·K^{-1} [3].

The theoretical prediction of near-field radiation between polar dielectric materials is dominated by surface phonon polaritons and the heat transfer is three orders of magnitude above the Planck's blackbody radiation limit at 30 nm gap between surfaces.

Shen et al [2, 3] used the AFM bi-material cantilever to measure the near-field radiation between a silica sphere and a silica substrate. Proximity approximation theorem was used for theoretical calculations for near-field radiation between sphere and substrate. In this system only a small part of the surface area of the sphere contributes to the near-field radiation. Hence, it is treated as near-field radiation between two parallel plates with surface areas of $2\pi Rd$ where R is the radius of the sphere and d is gap for the proximity approximation. After normalizing the areas, the near-field radiative heat transfer coefficient between silica and silica was calculated to be 2230 $W \cdot m^{-2} \cdot K^{-1}$ at 30 nm gap compared to the 3.8 $W \cdot m^{-2} \cdot K^{-1}$ of the blackbody radiation limit. Using this technique [3], the near-field radiation was also measured between silica sphere and different substrates as silicon, gold and silica.

1.4 Objectives

The main objective of this thesis is to understand and measure the near-field radiation using custom designed thermal metrology with AFM bi-material cantilevers. The main aim of this thesis is to validate the technique used by Shen et al [2, 3] and use it to measure the near-field radiation between silica microsphere and silicon carbide and compare it with theoretical calculations. A silica sphere with 100 μm diameter will be attached to the AFM cantilever and the near-field radiative heat transfer between the silica sphere and silica or SiC substrates will be measured with vacuum gaps from a few micrometers to a few tens of nanometers.

CHAPTER 2 THEORETICAL METHODS

2.1 Theoretical Model for Determining AFM Cantilever Thermal Conductance due to Conduction

The AFM cantilever used here is made of silicon nitride (450 nm thickness) with a gold coating of 70 nm in thickness. Although the cantilever has triangular shape, we model the cantilever as a rectangular beam to simplify the analysis [33]. Based on the Euler-Bernoulli beam theory and thermal analysis, the deflection of the bi-material cantilever can be solved using the following equations [26, 34, 35]:

$$\frac{d^2Z}{dx^2} = 6(\gamma_2 - \gamma_1)\frac{t_1+t_2}{t_1 t_2 K}[T(x) - T_0] \tag{2.1}$$

$$K = 4 + 6\left(\frac{t_1}{t_2}\right) + 4\left(\frac{t_1}{t_2}\right)^2 + \frac{E_1}{E_2}\left(\frac{t_1}{t_2}\right)^3 + \frac{E_2}{E_1}\left(\frac{t_2}{t_1}\right) \tag{2.2}$$

where t_1 and t_2 are the thickness of the layers (Si_3N_4, $t_1 = 450$ nm and Au, $t_2 = 70$ nm), γ_1 and γ_2 are the thermal expansion coefficient of layers 1 and 2 respectively, $Z(x)$ is the vertical deflection at any given location x, E_1 and E_2 are the Young's Modulus of layers 1 and 2 respectively, $T(x)$ is the temperature distribution along the cantilever and T_0 is the ambient temperature.

To calculate the thermal conductance of the AFM cantilever two calibrations are required:

1. The sensitivity of the cantilever with respect to change in absorbed power.

2. The sensitivity of the cantilever with respect to change in ambient temperature.

For the 1st calibration, consider that setup is placed in vacuum and the laser beam is focused on the tip of the AFM cantilever as shown in Fig. 2.1:
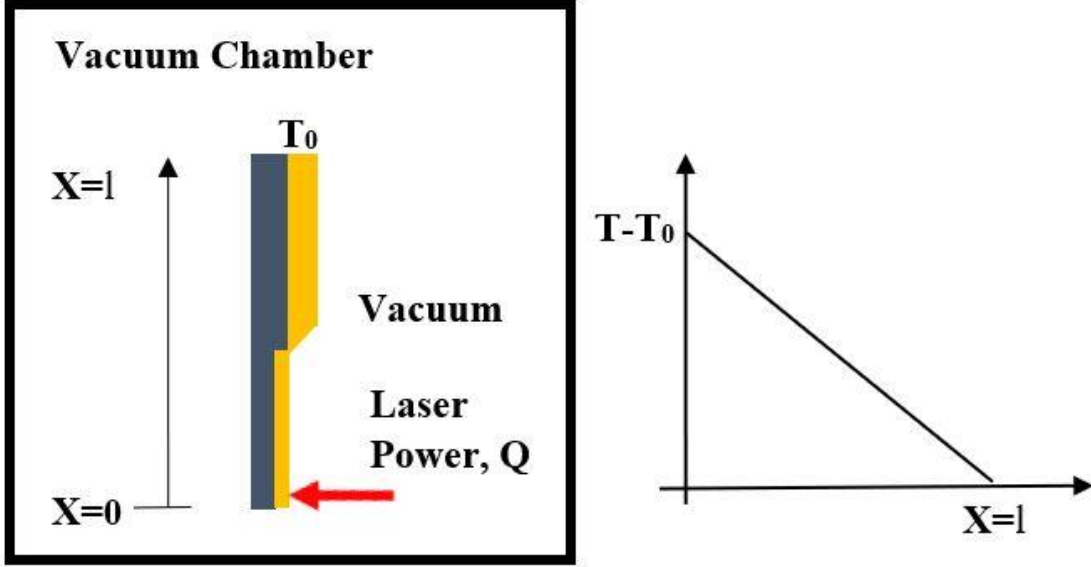
Figure 2.1: Schematic and Steady-State Temperature Profile of the Cantilever when Heated with a Laser Focused on the Tip in Vacuum

The temperature distribution for this case is given by

$$T(x) - T_0 = \left(1 - \frac{x}{l}\right)\frac{Q_{abs}}{G} \qquad (2.3)$$

where Q_{abs} is the power absorbed by the cantilever tip, G is the thermal conductance of the cantilever and l is the total length of the cantilever. Using the translation stages the laser is focused on to the cantilever tip without disturbing the CCD camera focus. To remove the air conduction and convection the experiment needs to be done in vacuum. The tip absorbs certain amount of laser power depending on the absorptance of the tip. As the cantilever is bi-material it deflects due to the laser heating. Using the temperature distribution in the Eq. 2.1, the slope of the cantilever is given by

$$\frac{dZ(0)}{dx} = \frac{-3lQ_{abs}H}{G} \qquad (2.4)$$

where
$$H = \frac{(\gamma_2 - \gamma_1)(t_1 + t_2)}{t_1 t_2 K}$$

10

As the deflection angle (also the slope of the cantilever) is too small it is approximately half of the deviation angle of the laser beam.

$$\frac{dZ(0)}{dx} = \frac{0.5\Delta d}{s} \tag{2.5}$$

where Δd is the displacement of the lase spot on the PSD and s is the optical path distance between the cantilever tip and the PSD. So, by combining the slope and deflection angle of the cantilever we get the sensitivity of the cantilever by changing the absorbed power is:

$$\Delta d = \frac{-6lQ_{abs}Hs}{G} \tag{2.6}$$

$$S_Q = \frac{\partial(\Delta d)}{\partial Q_{abs}} = \frac{-6slH}{G} \tag{2.7}$$

As the thermal conductance of the cantilever G is unknown at this stage we need to calculate the sensitivity with respect to change in absorbed power through experiment. The time constant for the cantilever to reach steady state deflection is approximately 1 milli second [26].

For the 2$^{\text{nd}}$ calibration, the sensitivity with respect to ambient temperature is to be determined. Here the laser power is kept constant while the ambient temperature is varied. The setup is placed in ambient where the temperature is controlled at temperature T_b. The temperature of the cantilever base is assumed to be T_b In this case the cantilever still has a temperature distribution due to the incident laser power at the tip. As the cantilever is very thin compared to its length it is analyzed as a fin with a natural convection heat transfer coefficient h. The temperature profile is given by:

$$T(x) - T_b = \frac{Q_{abs}}{G} \frac{\sinh[\beta(l-x)]}{\beta l \cosh(\beta l)} \tag{2.8}$$

where β is the fin parameter given by $\sqrt{\dfrac{2h(w+t_1+t_2)}{lG}}$, w is the effective width. The natural convective coefficient is assumed to be 500 $W \cdot m^{-2} \cdot K^{-1}$ or larger due to small geometry of the cantilever [36]. Fig. 2.2 shows the schematic of the setup and the profile of the temperature distribution.
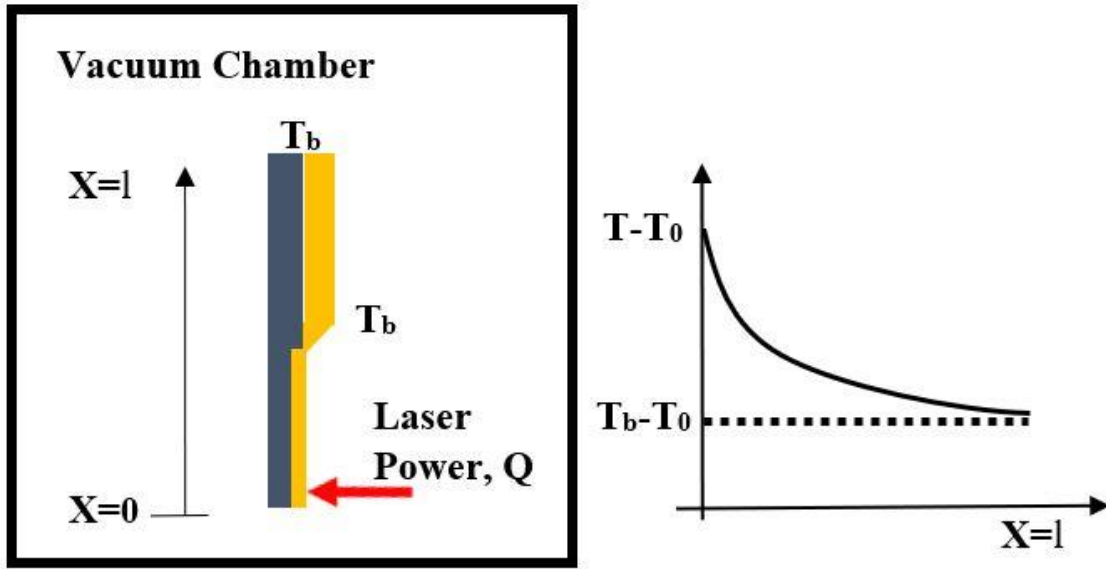
Figure 2.2: Schematic and Steady-State Temperature Profile of the Cantilever when Heated with a Laser Focused on the Tip in Air at Temperature T_0

The slope at the tip or the deflection angle of the cantilever is calculated using the Eq. 2.1 and is given by:

$$\frac{dZ(0)}{dx} = -6H\left\{(T_b - T_0)l + \frac{Q_{abs}}{G}\frac{[-\text{sech}(\beta l)]}{\beta^2 l}\right\} \tag{2.9}$$

Now, the sensitivity of the cantilever with respect to change in ambient temperature is calculated from Eqns. 2.4 and 2.9 and is given by:

$$S_T = \frac{\partial(\Delta d)}{\partial T_b} = -12sHl \tag{2.10}$$

From Eqns. 2.7 and 2.10 the thermal conductance of the cantilever is determined to be:

$$G = 0.5 \frac{S_T}{S_Q} \tag{2.11}$$

2.2 Calculation of the Tip or Sphere Temperature without Near-Field Effect

After determining the thermal conductance G, the tip temperature needs to be calculated. The tip and sphere temperatures are assumed to be approximately the same with thermally conductive paste used for attaching sphere onto the tip. A microsphere is attached to tip to increase the surface area available for near-field radiation heat transfer between the substrate and tip. Also, same dielectric materials (silica sphere and silica substrate) are used to increase the near-filed coupling effect with surface phonon polaritons. The tip temperature is calculated when the distance between the substrate and the tip is $\geq 10\ \mu m$ without near-field radiation in effect. Considering that the setup is placed in vacuum and assuming that the cantilever base, vacuum chamber walls and all other devices inside the chamber are at the same temperature T_0.
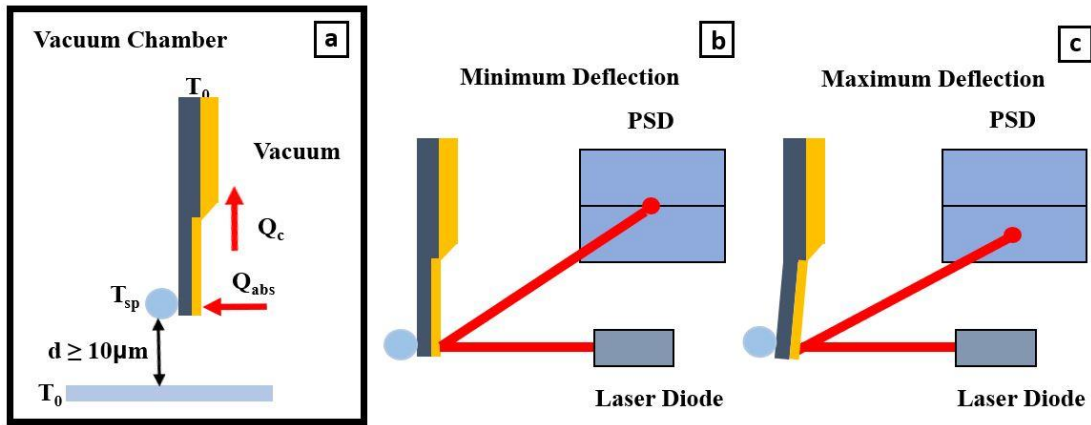
Figure 2.3: (a) Schematic of the Setup for Measuring Sphere/Tip Temperature without Near-Field Effect, Schematic of Position of Laser Beam Spot on PSD at (b) Minimum Laser Power and (c) Maximum Laser Power

The schematic of the setup is shown in Fig. 2.3(a), where Q_{abs} is the absorbed power, Q_c is the power conducted through the cantilever and d is the distance between the microsphere and substrate. The Fig. 2.3(b) and (c) shows the laser beam spot on the PSD

at minimum and maximum laser when the distance is greater than 10 μm. The laser beam spot is focused at the center of the PSD at the minimum power. As the laser power is increased the AFM cantilever bends and the laser beam spot is shifted away from the center of the PSD. As the distance is greater than 10 μm the near-field radiation is not in effect. The only heat transfer is the conduction through the cantilever by neglecting the far-field radiation, and then the energy balance gives:

$$Q_{abs} = Q_c = G(T_{sp} - T_0) \tag{2.12}$$

Then the microsphere or tip temperature T_{sp} can be calculated from:

$$T_{sp} = \frac{Q_{abs}}{G} + T_0 \tag{2.13}$$

2.3 Calibration Procedures for AFM Bi-Material Cantilevers

The bending and absorbed power of the AFM cantilever are determined from the PSD signals. There are two outputs from PSD that can be used: sum signal (0 to 6V) and Y difference signal (-10V to 10V). The PSD sum signal represents the reflected laser power by the AFM cantilever, and the PSD difference signal represents the position change of the laser spot on the PSD due to AFM deflection.

As the experiment is conducted in a vacuum chamber, the only data to be collected during the experiment is the PSD sum and difference signals. To calculate the absorbed power based on the sum signal of PSD, the AFM cantilever is calibrated by varying the laser power with the help of laser diode driver. The absorbed power of the cantilever can be calculated from the PSD sum signal by using the expression below:

$$Q_{abs} = V_{sum} \times \left(\frac{\partial Q_r'}{\partial V_{sum}}\right) \times \left(\frac{1}{\tau_{optics}}\right) \times \left(\frac{\alpha_{Au,AFM}}{\rho_{Au,AFM}}\right) \tag{2.14}$$

14

where V_{sum} is the PSD sum signal, and $\frac{\partial Q'_r}{\partial V_{sum}}$ is the slope of the correlation between the reflected laser powers at the PSD location by equation $Q'_r = (Q_i - Q_{sr})\rho_{Au,AFM}\tau_{optics}$ and the corresponding PSD sum signals. Note that Q_i could be either premeasured with a power meter between the objective and probe if laser power is fixed or calculated based on Fig. 3.6 from numbers of trim pot turns.

Also, the slope of the correlation between PSD difference signals and the corresponding absorbed powers gives the sensitivity with respect to change in absorbed power, which is $\frac{\partial(\Delta d)}{\partial Q_{abs}} = S_Q$.

The sensitivity to the ambient temperature is measured experimentally by placing the setup inside the closed vacuum chamber and increasing the air temperature near the AFM probe using a thermoelectric cooler (TEC, TES1-7103). The TEC is powered with a DC power supply (Circuit Specialists, CSI12001X) at constant voltage and current. The cold side of the TEC is placed on a large Al block heat sink and a translation stage, while hot side is facing towards the AFM probe at a close distance with the translation stage. As the result, the surface temperature of the hot side increases by increasing the voltage input to the TEC. The ambient temperature is measured using a resistance temperature detector (RTD) placed very close to the cantilever base. The temperature change at the base is assumed to be much slower than the relaxation time (steady state deflection) of the cantilever. The PSD difference signal gives the deflection change of the cantilever as the ambient temperature is increasing. The slope of the correlation between PSD difference signal and the ambient temperature change gives the sensitivity to the ambient temperature change i.e., $S_T = \frac{\partial(\Delta d)}{\partial T_b}$.

After both S_Q and S_T are experimentally measured, the thermal conductance G of the cantilever can be found using Eqn. 2.11 as $G = 0.5 \frac{S_T}{S_Q}$.

2.4 Theoretical Model for Determination of Thermal Conductance due to Near-Field Radiation

When the distance between the sphere and substrate is less than 10 μm the near-field radiation starts to take effect due to the tunneling of the evanescent waves. Fig. 2.4 (a) illustrates the heat transfer when the sphere is close to the substrate with near-field radiation in effect and (b) shows the change in position of laser beam spot on PSD due to near-field radiation effect, where the setup is placed in vacuum and the cantilever base and vacuum chamber wall are assumed at the same temperature T_0.
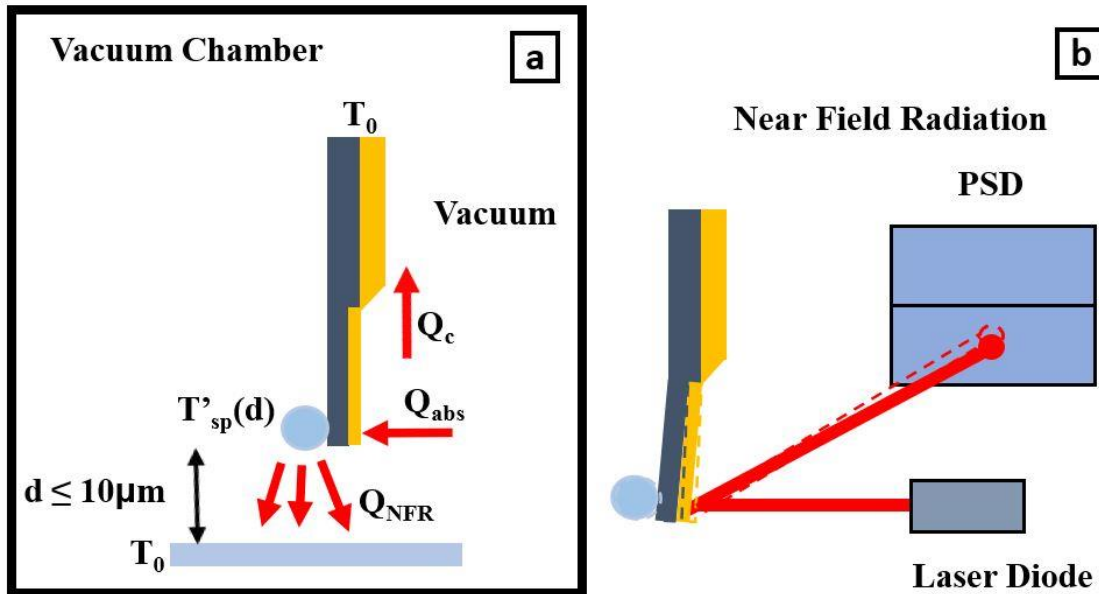
Figure 2.4: (a) Schematic of the Setup for Measuring the Conductance due to Near-Field Radiation and (b) Schematic of the Change in Position of Laser Beam Spot on the PSD due to Near-Field Effect

Although the far-field radiation is always in effect and a view factor of 1 can be assumed between the sphere and substrate when the gap distance is much smaller than the

16

sphere diameter, far-field radiation is considered negligible when compared to the conduction through the cantilever. So, any changes in the sphere temperature, which is monitored by the PSD difference signal from cantilever deflection change, is mainly caused by the near-field radiation when the substrate is brought closer and closer towards the microsphere. Hence the energy balance at steady state gives:

$$Q_{abs} = Q_c + Q_{NFR} = G\left[T'_{sp}(d) - T_0\right] + G_{NFR}\left[T'_{sp}(d) - T_0\right] \tag{2.15}$$

where G_{NFR} is the conductance of the near-field radiation to be found and $T'_{sp}(d)$ is the new sphere temperature at a given gap distance d in μm controlled by the piezo stage.

The distance between substrate and sphere is approximately 10 μm determined from optical image by the CCD camera before pumping down. As the near-field radiation is negligible at this distance and the thermal conductance of the cantilever G is constant the sphere temperature $T'_{sp}(10)$ can be calculated using Eq. 2.13. When the vacuum pressure reaches 0.1 Pa, the near-field measurement will start by moving the substrate closer to the microsphere using the piezo motion control stage (Mad City Labs, Nano-OP30) at a step of 50 nm. Both PSD difference and sum signals at a given gap distance will be recorded. PSD sum signal is expected to be constant, which ensures that the incident laser power and absorbed one Q_{abs} is stable, while the PSD difference signal changes indicate sphere temperature change due to near-field radiation effect. In particular, the approaching will stop when the substrate is in physical contact with the microsphere indicated by a sudden jump from the PSD difference signal due to abrupt temperature change of conduction between the two. The new sphere temperature is calculated using the sensitivity of the cantilever with respect to change in ambient temperature i.e., S_T. Here it is assumed that the cantilever sensitivity when in ambient and vacuum is approximately

the same. If $V_{diff,10}$ and $V_{diff,d}$ are the PSD difference signals at 10 μm distance and distance d respectively, the new sphere temperature at a given distance d can be calculated from the PSD difference signals as

$$T'_{sp}(d) = \frac{V_{diff,d} - V_{diff,10}}{S_T} + T'_{sp}(10) \qquad (2.16)$$

Once the new sphere temperature at distance d is calculated, the $G_{NFR}(d)$ can be found from

$$G_{NFR}(d) = \frac{Q_{abs}}{T'_{sp}(d) - T_0} - G \qquad (2.17)$$

CHAPTER 3 EXPERIMENAL SETUP AND CALIBRATION OF THE

CANTILEVER

3.1 Experimental Setup

A schematic of the experimental setup is shown in Fig. 3.1. The laser beam from a semiconductor laser diode is transmitted through a collimation lens (Thorlabs, A230TM-B, f = 4.51 mm) and an iris (Thorlabs, CP20S) before entering the polarizing beam splitter (Thorlabs, CCM1-PBS251). The laser diode is connected to a laser diode driver kit (Thorlabs, EK1101) with an electrostatic discharge protection and strain relief cable (Thorlabs, SR9A) to control the laser power output as required. The laser driver kit is connected to a DC power supply (Keithley, 2200-30-5) to power the laser diode with a constant voltage and current.
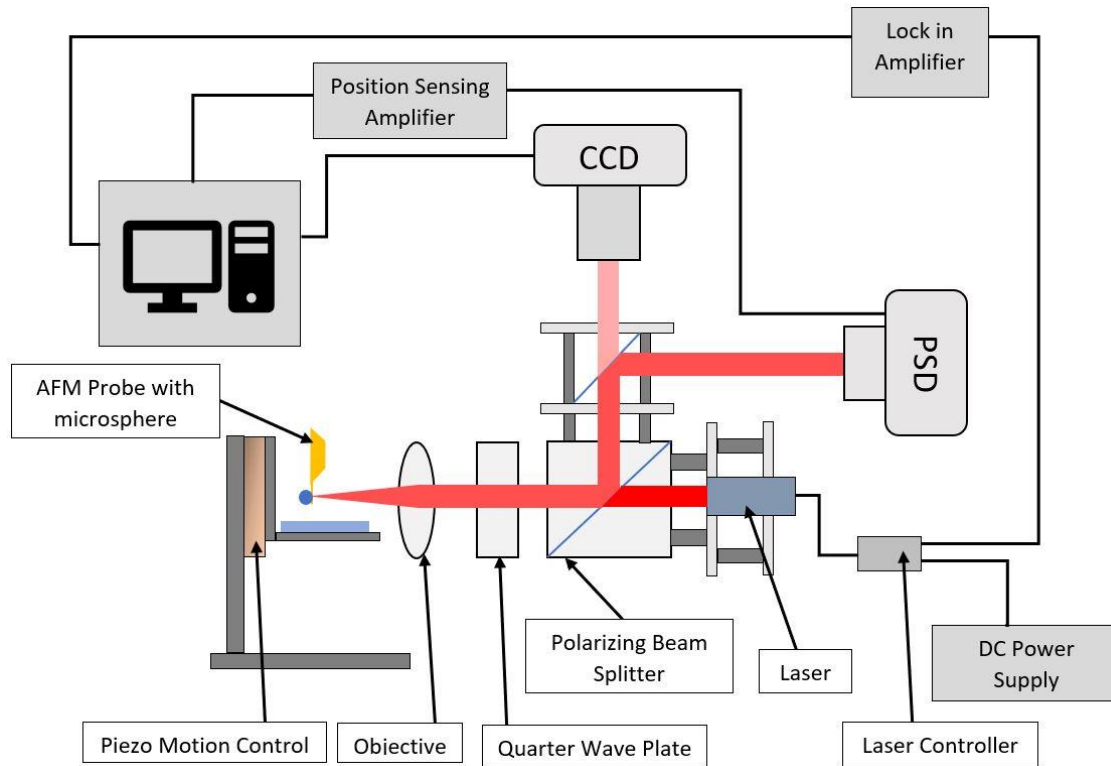
Figure 3.1: Schematic of the Experimental Setup

As the laser output is linearly polarized, only p-polarized beam passes through the beam splitter and s-polarized beam is reflected. The p-polarized beam is rotated 45° after it transmits through the quarter-wave plate (Thorlabs, WPMQ05M-670), which makes it circularly-polarized beam. The laser beam is focused on the AFM cantilever tip (Budget Sensors, SiNi) with the help of a 20× microscope objective. The cantilever is positioned perpendicular to the substrate with a tolerance of +/-2° to avoid the bending of cantilever due to dispersion and electrostatic forces between the AFM cantilever and the substrate.

The normally reflected laser beam from the gold-coated AFM cantilever is transmitted through the same quarter-wave plate and rotated by 45° again. This makes the beam s-polarized which is reflected by the same polarizing beam splitter. The combination of polarizing beam splitter and a quarter-wave plate reduces the ghost image formation. After the polarizing beam splitter, the beam is incident on a 90:10 plate beam splitter (Thorlabs, BSX10) where only 10% of the beam is sent to the CCD camera (AmScope, MU1000) and 90% is reflected to the position sensitive detector (ON-TRAK Photonics, PSM2-10). The reflected beam forms a spot on the PSD, where the position and power of the laser beam are obtained from the difference and sum signals of the PSD respectively with a position sensing amplifier (ON-TRAK Photonics, OT-301) recorded by a computer with a custom LabVIEW program through a data acquisition card (National Instruments, NI PCIe-6259) and a shielded BNC connector block (National Instruments, BNC-2110). Figs. 3.2 and 3.3 show the Solidworks model and a photo of assembled setup.

As shown in Fig. 3.4, the AFM probe is attached with a double-sided tape to a probe holder bolted to a motion control stage (Thorlabs, MT1) with a resolution of 0.5 μm by a differential adjuster (Thorlabs, DM10). The substrate is placed on L-Bracket (McMaster-

Carr, 2313N55) which is attached to a piezo motion control stage (Mad City Labs, Nano-OP30) with 30 μm range and 0.1 nm resolution controlled by a piezo controller (Mad City Labs, Nano-Drive). The cantilever absorbs a portion of incident laser beam while the rest is reflected at its tip. This causes a temperature rise of the cantilever tip, which in turn bends the bi-material cantilever due to mismatch of thermal expansion coefficients between SiNi and Au. The base of the cantilever, the substrate and the rest of the setup are at the ambient temperature. The cantilever beam deflection is measured from the position change of the beam spot on the PSD.

As shown in Fig. 3.5, the entire setup is placed inside an 18-inch vacuum chamber with several feedthrough ports, and a turbomolecular pump (Agilent, TPS-Flexy TwisTorr 74 FS) which can reduce the chamber pressure down to 5×10^{-8} Pa. The experiment requires a pressure of 6×10^{-3} Pa but due to outgassing from the setup devices the time required to reach the same is considerably large. It takes approximately 6 hours to reach 1×10^{-1} Pa. Also, the theoretical calculation suggests that a vacuum pressure below 1×10^{-1} Pa is low enough to have negligible conduction and convection with air molecules compared to the near-field radiation between silica [37]. When the gap between the sphere and substrate decreases, the temperature of the cantilever is expected to decrease with fixed laser power as the heat transfer from the cantilever to the substrate increases due to the near-field radiation effect. The resultant cantilever deflection due to decreased temperature is measured by PSD difference signal, from which the near-field conductance vs. gap distance curve can be obtained.
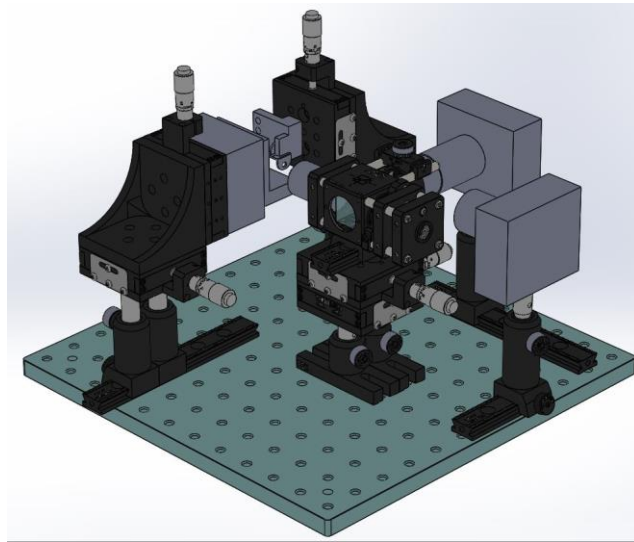
Figure 3.2: Solidworks Assembly Model of Experimental Setup.
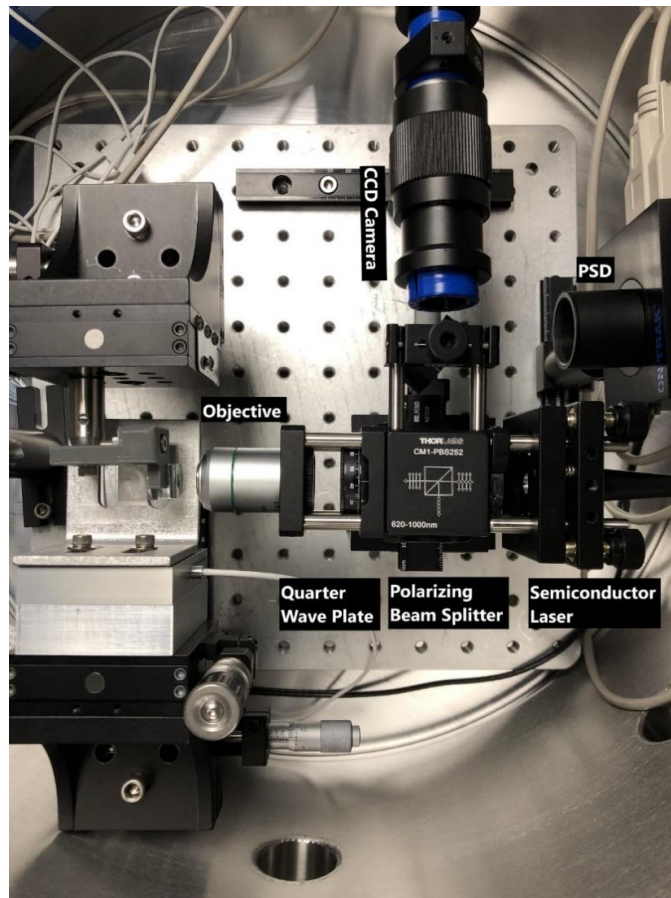
Figure 3.3: Top View of Experimental Setup Inside Vacuum Chamber.
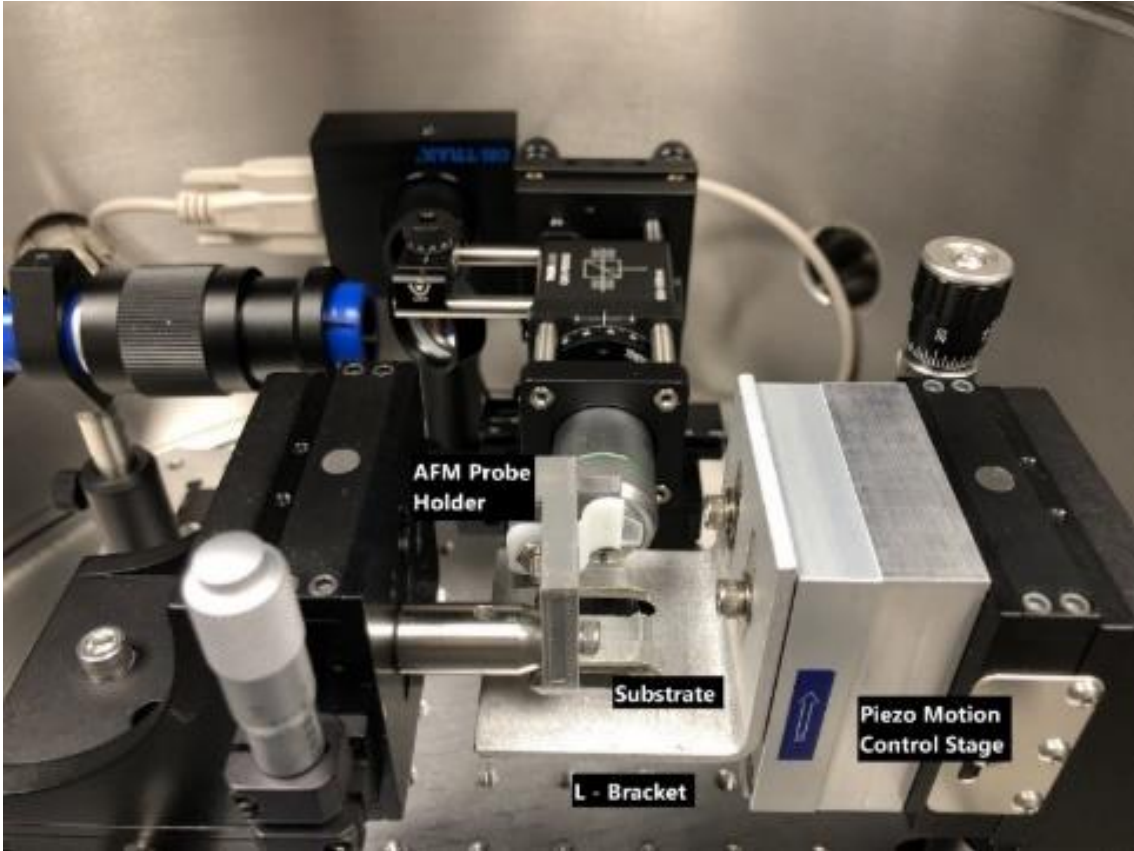
Figure 3.4: Experimental Setup Picturing the Substrate, L-Bracket and Piezo Motion Control

Figure 3.5: (Left) Vacuum Chamber and (Right) Vacuum Pump

3.2 Experimental Procedures for Cantilever Calibration

All the required procedures to determine the thermal conductance of AFM cantilever are depicted in the following flow chart.

Adjust the laser diode such that maximum power is transmitted through the polarizing beam splitter

↓

Calibrate the laser power with respect to the numbers of trim pot turns on the laser drive kit

↓

Attach the aluminum mirror and AFM probe to the probe holder

↓

Focus the CCD camera on the AFM probe and the aluminum mirror

↓

Determine the transmittance of the optics for the setup

↓

Align and focus the laser beam onto the tip of AFM cantilever

↓

Find the reflectance and absorptance of the AFM cantilever

↓

Correlate the reflected laser power and PSD sum signal

↓

Correlate the PSD deflection signal of the AFM cantilever with absorbed power

↓

Fit the PSD deflection signal of the AFM cantilever with ambient temperature

↓

Determine the thermal conductance of the cantilever

3.3 Laser Focusing and Power

Two different semiconductor laser diodes with maximum powers of 10 mW (Thorlabs, HL6748MG) and 15 mW (Thorlabs, HL6756MG) both with a wavelength of 670 nm are used during the measurements to both heat the AFM cantilever and determine the temperature of the cantilever due to deflection through PSD. The two different lasers are not used simultaneously. The laser needs to be focused on the tip such that entire laser beam is incident on the tip. The optical imaging with CCD camera and laser focusing share the same light path, while the focusing should be done without disturbing the CCD camera image clarity. The system setup has necessary motion stage controls for adjusting the laser focus without disturbing the CCD focus.

The polarizing beam splitter along with the quarter wave plate is used to avoid ghosting problem in the CCD image. Also, a 90:10 (reflectance : transmittance) beam splitter is used in front of the CCD camera to not saturate it. While the laser output is linearly polarized, the laser beams electric field plane needs to be in the same plane as the polarizing beam splitter to get maximum power transmittance. The maximum power from the laser can be transmitted through the polarizing beam splitter by aligning the plane of incidence of the laser beam with the beam splitter parallel plane. This can be achieved by rotating the laser setup and measuring the laser power with a photodiode power sensor (Thorlabs, S120C) and a power meter (Thorlabs, PM100D) to check at which position maximum power is transmitted. Hence the laser diode setup is rotated in the 30 mm cage system such that maximum power is transmitted through the beam splitter.

Fig. 3.6 shows the laser powers through the objective of the setup at the minimum iris diameter, which is incident on the AFM cantilever, at every turn of the trim pot for

laser diodes HL6748MG and HL6756MG respectively. The monitoring current is set to 1 mA for HL6748MG laser diode and 1.5 mA for HL6756MG and based on the monitoring current based on the gain resistors set as per the EK1101 laser driver kit manual. The maximum number of trim pot turns to reach the maximum power for HL6748MG (10 mW) and HL6756MG (15 mW) laser diodes is 11 and 7 approximately for 1 mA and 1.5 mA monitoring currents respectively.
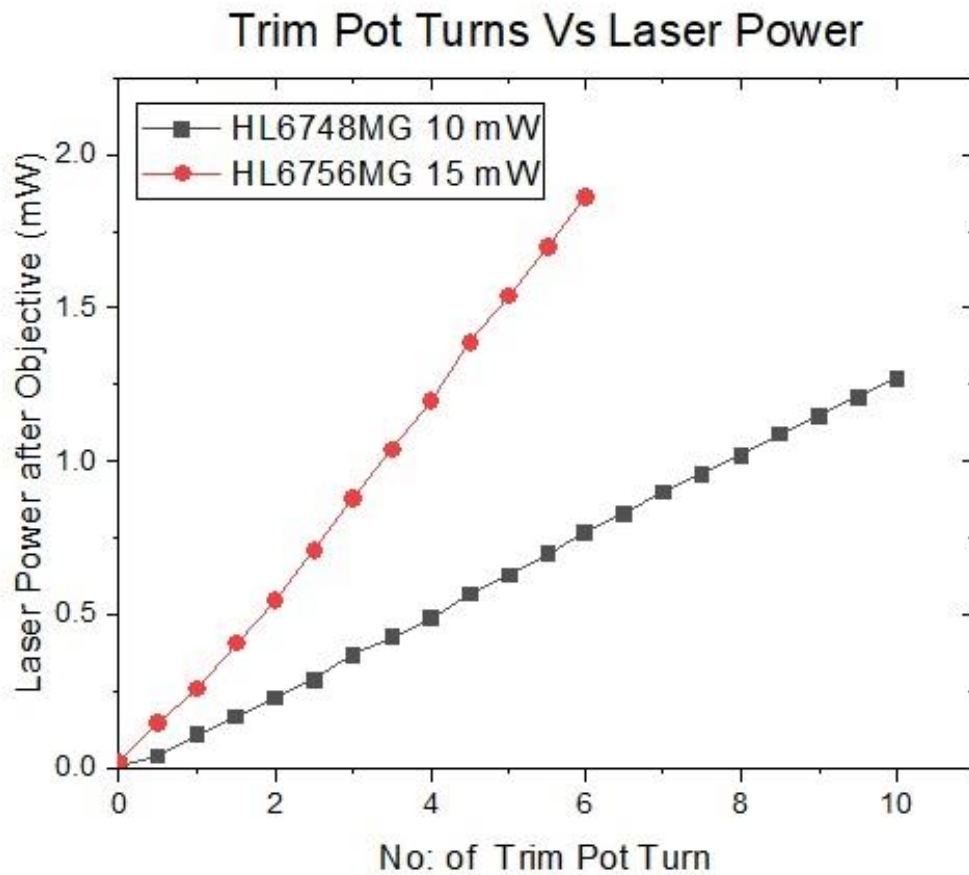
Figure 3.6: Measured Laser Power after Objective as a Number of Trim Pot Turns for Different Laser Diodes (Thorlabs HL6748MG and HL6756MG).

3.4 Working Principle of Position Sensitive Detector (PSD)

As the only data available during the experiments is PSD sum and difference signal the mechanism of the PSD is explained here. The PSD used here consists of n-type silicon substrate with two resistive layers separated by a p-n junction. The front side is an p-type resistive layer with two contacts at opposite ends. Similarly, the back side is n-type resistive layer with two contacts at opposite ends which are placed orthogonally to the contacts on the front side. The laser spot which is in the spectral range of the silicon generates a photocurrent that flows from the incident spot through the resistive layers to the electrodes placed at the contacts. As the resistive layers are extremely uniform, the photogenerated current at each electrode is inversely proportional to the distance between the incident spot of laser and electrodes. The PSD outputs track the motion of the centroid of power density. The position sensing amplifier (ON-TRAK Photonics, OT-301) takes the photocurrent from each electrode and process the signals to provide the sum and difference signals. The Fig. 3.7 shows the schematic of the PSD along with the equation used to provide the X and Y position of the laser spot.

$$X = \frac{X_1 - X_2}{X_1 + X_2} \times \frac{L}{2}$$

$$Y = \frac{Y_1 - Y_2}{Y_1 + Y_2} \times \frac{L}{2}$$
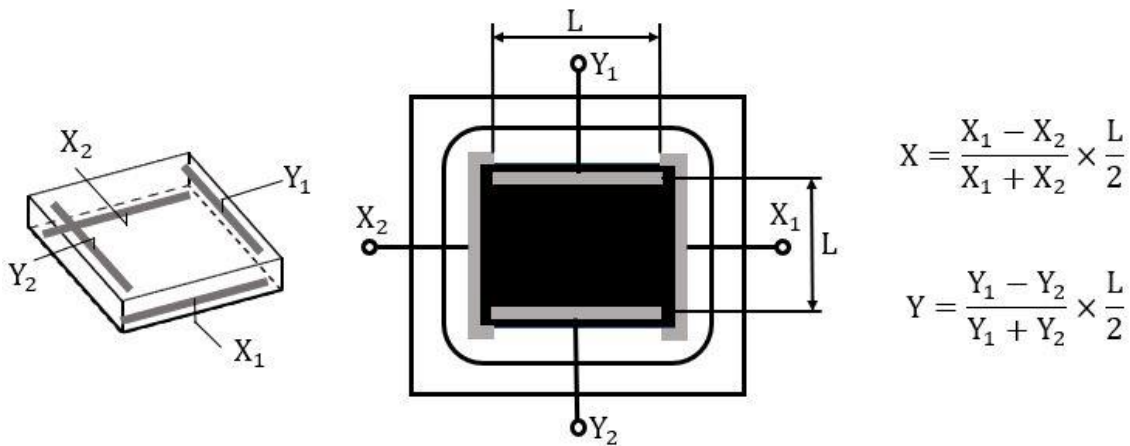
Figure 3.7: Schematic of PSD and the Equations for the X and Y Position of the Laser Spot

27

3.5 Transmittance of the Optical Setup, Reflectance and Absorptance of the AFM Cantilever

To calculate the heat absorbed from the incident laser beam by the cantilever, the absorptance of the cantilever needs to be determined. Laser powers are measured at different locations using a power meter as illustrated in Fig. 3.8. From the schematic of the experimental setup it is clear that there will be optical loss due to the optical parts. As the laser transmits through various optical parts there will be power loss. To calculate the optical transmittance of the setup an aluminum sample (230 nm Al deposited on a polished silicon wafer) is used as a mirror and the transmittance of the setup is calculated using the following equation:

$$\tau_{\text{optics}} = \frac{Q_r'}{(Q_i - Q_{sr})\rho_{Al}}$$

(3.1)

where Q_i is the incident laser power, Q_{sr} is the strayed beam power, and Q_r' is the reflected laser power through the optics at the location of PSD after the 90:10 plate beam splitter. ρ_{Al} is the reflectance of the aluminum mirror, which is calculated to be 0.9098 at 670 nm wavelength based on Palik's data for the optical constants of Al. The aluminum mirror and AFM probe are attached to the same probe holder so as not to disturb the system optics. The laser beam is focused on to the Al mirror from the CCD camera by using the translation stage along with a differential adjuster.
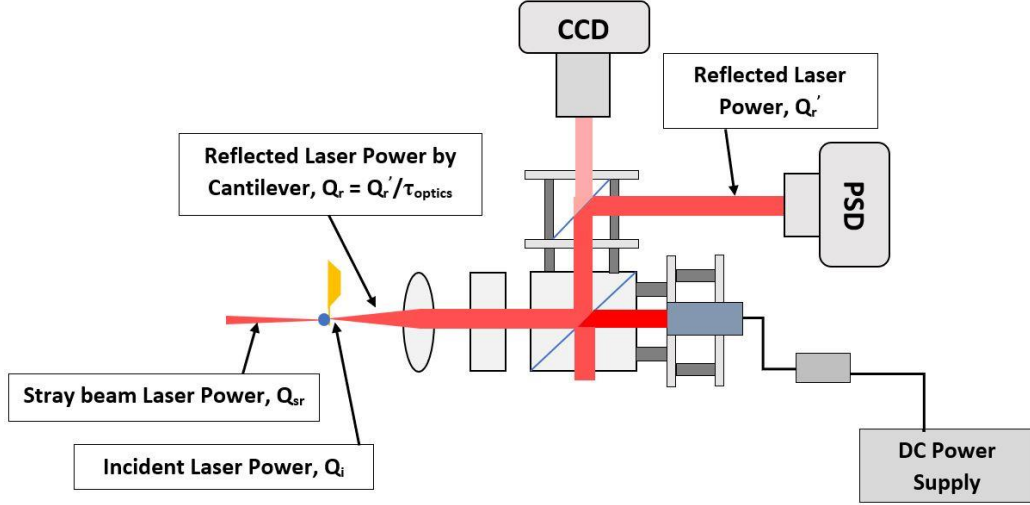
Figure 3.8: Schematic of Optical Power Measurements at Multiple Locations in Order to Find the Transmittance of the Optical Setup, Reflectance and Absorptance of the Gold Coated AFM Cantilever

After the optical transmittance of the system is determined using Eq. 3.1, laser beam is focused on to the AFM cantilever tip with gold coating, which reflects the beam to PSD. After calculating the reflected laser power in front of the PSD, the reflectance of the Au coating is calculated from the equation:

$$\rho_{\text{Au,AFM}} = \frac{Q_r'}{(Q_i - Q_{sr})\tau_{\text{optics}}}$$ (3.2)

and the absorptance of the cantilever is calculated from the below equation as it is opaque:

$$\alpha_{\text{Au,AFM}} = 1 - \rho_{\text{Au,AFM}}$$ (3.3)

The absorbed power by the cantilever tip Q_{abs} can be determined now from equation below:

$$Q_{abs} = \alpha_{Au,AFM}(Q_i - Q_{sr})$$ (3.4)

3.6 Procedures to Attach Microsphere onto AFM Bi-Material Cantilevers

The AFM probe used here is a SiNi AFM probe from Budget Sensors which is the same probe used by Shen et al [2]. The probe base is made of silicon with dimensions as $3.4 \times 1.6 \times 0.45$ mm^3. The probe has 2 long and 2 short cantilevers which are triangular in shape. The length of the long and short cantilevers are 200 μm and 100 μm respectively. All 4 cantilevers are made up of two materials Si$_3$N$_4$ (thickness 520 nm) and Au (thickness 70 nm).
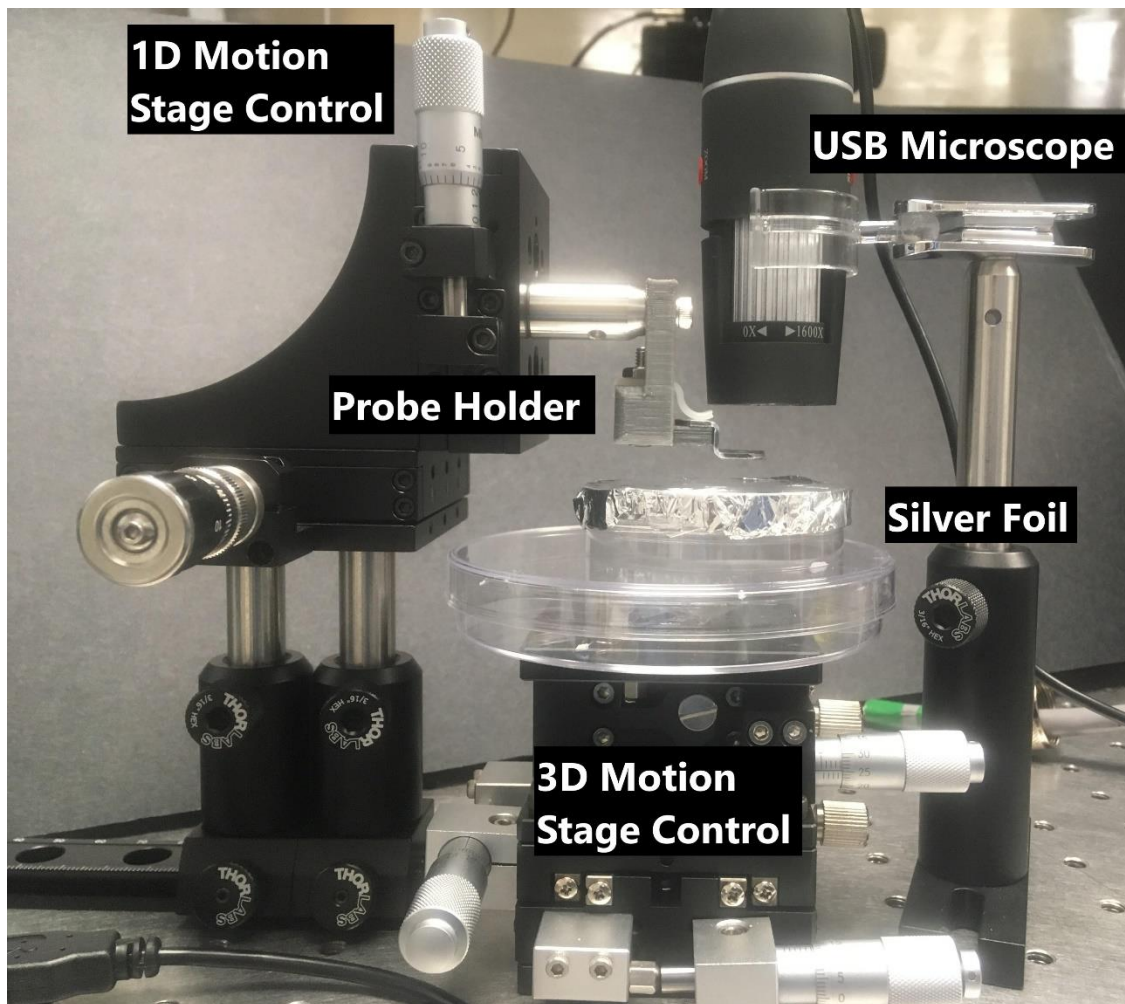
Figure 3.9: Photo of Setup used for Attaching Microsphere onto AFM Cantilever Tip

First the AFM cantilever tip needs to be attached with a 100 μm diameter silica microsphere (Corpuscular, 140280-10). The experimental setup to attach the sphere is shown in Fig. 3.9. The AFM probe is fixed to the probe holder which is mounted onto a translation motion stage. The thermal compound Arctic silver (Ceramique 2) is used to attach the sphere. A small drop of thermal compound is placed on the aluminum foil and the USB microscope is focused on the foil. Due to the high viscosity of thermal compound which might easily break the probe, isopropyl alcohol (IPA) was used to mix and to dilute the compound so that it can be easier to use. IPA will evaporate within a few minutes after applied to the AFM tip. Using the translation motion stage, the AFM cantilever is lowered on to the silver foil surface till the tip touches the thermal compound. The tip bends and reflects the light, which helps in identifying that the bottom of the tip is coated with thermal compound. Next step is to place a few silica microspheres on the foil and focus onto the spheres with the USB microscope. Once a single isolated microsphere is identified, lower the AFM cantilever onto the sphere. Due to Van der Waals force between the tip and the sphere, the probe bends which can be seen as a reflection change of light. The probe can be lowered a bit further to make sure the sphere attaches to the probe properly but not too much to avoid damaging the probe.
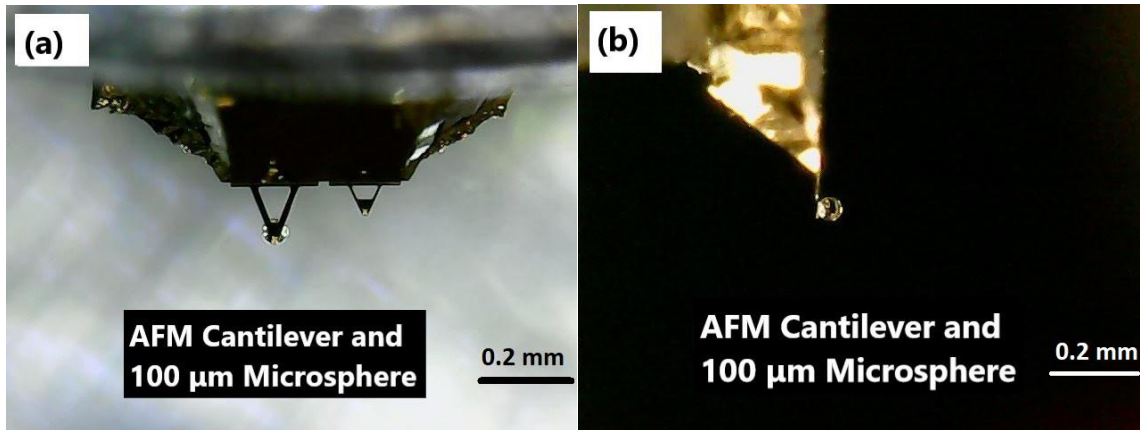
Figure 3.10: (a) Top and (b) Side View of an AFM Cantilever Attached with a 100-μm Silica Microsphere

After the microsphere is successfully attached onto the bottom of the cantilever, which is confirmed by optical microscope images as shown in Fig. 3.10, the probe holder is removed along with the cantilever and mounted onto the experimental setup inside the vacuum chamber for optical alignment and focusing of the laser beam. By using the CCD camera and motion control stages the laser beam is focused on to the AFM cantilever tip. The best optical alignment and focusing is indicated by the maximum sum signal from the PSD. The sample which is a glass slide for validation is brought closer to the microsphere by the manual translation stage till approximately 10 μm distance away seen with the CCD camera, which is then removed from the vacuum chamber as it causes outgassing problem in vacuum. When placing the cover plate on the vacuum chamber, PSD sum signal is monitored and should not change before and afterwards to make sure that the optical alignment is not disturbed by the possible vibrations during mounting the cover plate. It takes approximately 7 hours for the pressure to reach 0.1 Pa after the turbo pump is turned on.

3.7 Calibration Results for Different AFM Cantilevers

3.7.1 AFM Probe without Microsphere

All the calibrations for probe without microsphere are done using HL6756MG (15 mW) laser diode. The transmittance of the optics, reflectance and absorptance of the cantilever is calculated 3 times and average value is used for calculations. Table 3.1 shows the calculated average transmittance, reflectance and absorptance of the probe cantilever along with standard deviations.

Table 3.1: Transmittance, Reflectance and Absorptance of AFM Probe Cantilever without Microsphere

AFM Cantilever Probe without Microsphere	
Transmittance of the system	0.7439±0.0007
Reflectance of the AFM Cantilever	0.9714±0.0027
Absorptance of the AFM Cantilever	0.0286±0.0027
Ratio of Stray laser power to incident laser power	0.1809±0.004

Fig. 3.11 shows the calibration plots for AFM probe without microsphere including PSD sum signal variation as the reflected laser power changes (top), cantilever sensitivity for change in absorbed power (middle) and ambient temperature (bottom) respectively. Table 3.2 shows the calibration results determined as per the methodology in chapter 2 for probe without microsphere. The table also includes the fluctuations for PSD sum and difference signals.
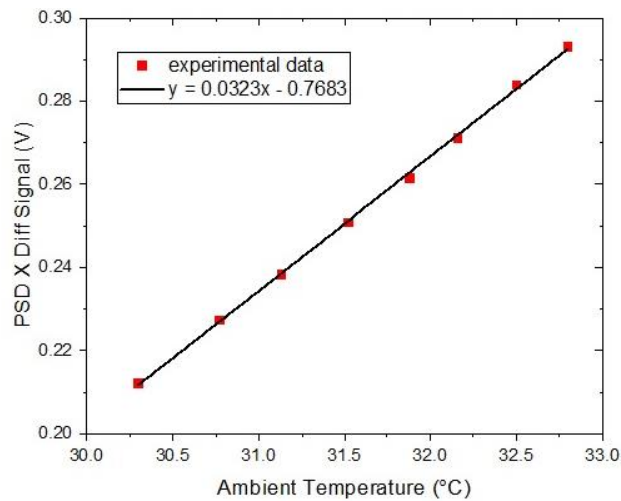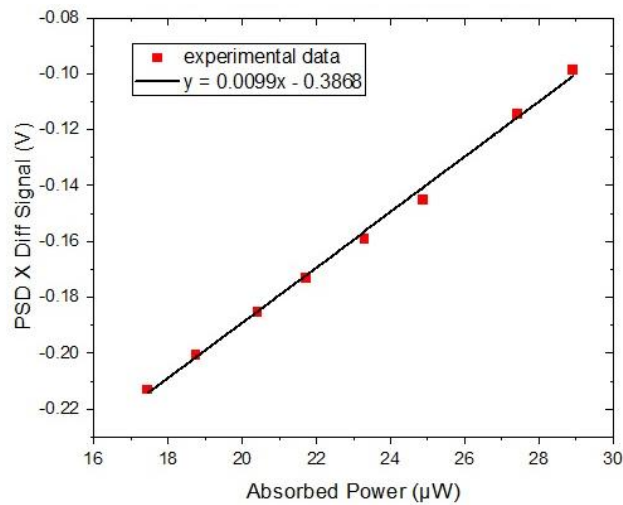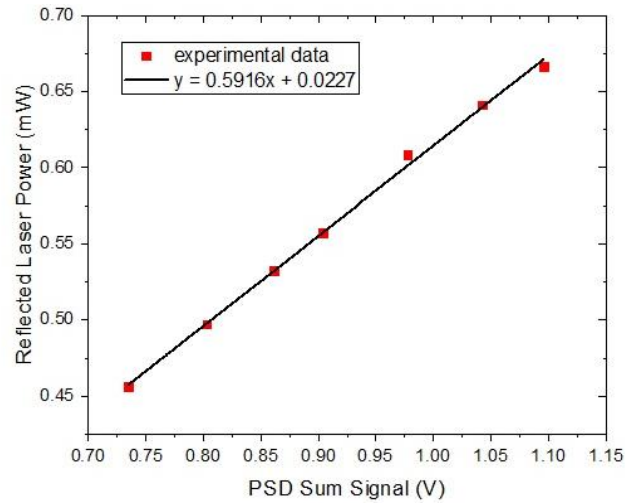
Figure 3.11: Calibration Plots for Probe without Microsphere: (Top) Reflected Laser Power vs. PSD Sum Signal; Sensitivity of AFM Cantilever with respect to Change in Absorbed Power (Middle) and Ambient Temperature (Bottom)

Table 3.2: Calibration Results for AFM Probe without Microsphere

Calibration results for probe without microsphere			
Plot	Absolute value of Slope	PSD Sum Fluctuation	PSD Diff Fluctuation
Reflected Laser Power vs. PSD Sum Signal (mW/V)	0.5916	0.05%	0.60%
Sensitivity of probe with respect to change in absorbed power, S_P (V/µW)	0.0099	0.05%	0.89%
Sensitivity of probe with respect to change in ambient temperature, S_T (V/°C)	0.0323	0.04%	0.63%

The vacuum pressure is in the range of 9.86×10^{-2} Pa to 9.11×10^{-2} Pa during the calibration of AFM sensitivity with respect to change in absorbed power. The thermal conductance is 1.6313 µW/°C which is calculated using Eq. 2.11. Also, the tip temperature is calculated using Eq. 2.13 for various absorbed powers while the setup is under vacuum, as shown in Fig. 3.12. The ambient temperature inside the vacuum chamber is 24.5°C.
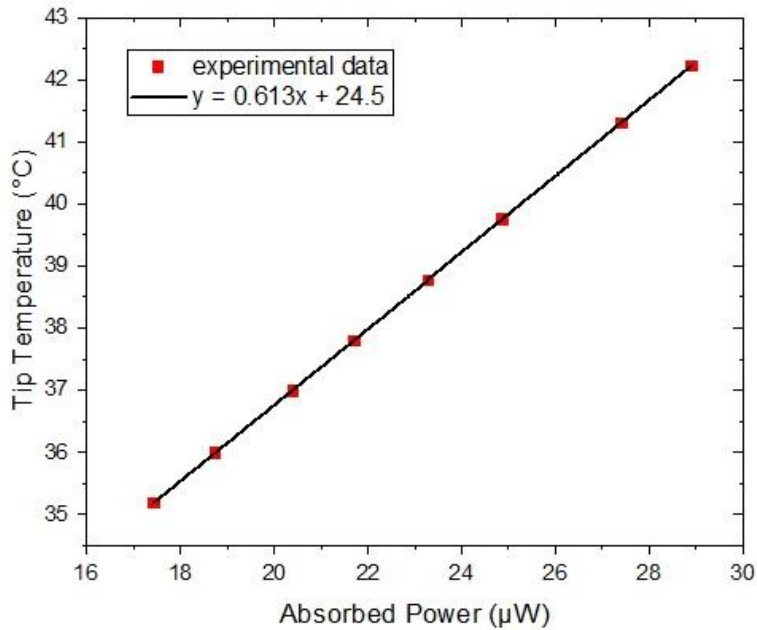
Figure 3.12: Tip Temperature vs. Absorbed Power in Vacuum for Probe without Microsphere

3.7.2 AFM Probe with Silica Microsphere

All the calibrations for probe with silica microsphere are done using HL6756MG (15 mW) laser diode. The transmittance of the optics, reflectance and absorptance of the cantilever is calculated 3 times and average value is used for calculations. The table 3.3 shows the calculated average transmittance, reflectance and absorptance of the probe cantilever.

Table 3.3: Transmittance, Reflectance and Absorptance of AFM Probe Cantilever with Silica Microsphere

AFM Cantilever Probe with Silica Microsphere	
Transmittance of the system	0.7207 ± 0.0024
Reflectance of the AFM Cantilever	0.8608 ± 0.0013
Absorptance of the AFM Cantilever	0.1392 ± 0.0013
Ratio of Stray laser power to incident laser power	0.0833 ± 0.0001

Table 3.4: Calibration Results for AFM Probe with Silica Microsphere

Calibration results for probe with silica microsphere			
Plot	Absolute value of Slope	Avg PSD Sum Fluctuations	Avg PSD X Diff Fluctuations
Reflected Laser Power Vs PSD Sum Signal (mW/V)	0.6204	0.04%	0.41%
Sensitivity of probe with respect to change in absorbed power, S_P (V/μW)	0.002	0.05%	0.23%
Sensitivity of probe with respect to change in ambient temperature, S_T (V/°C)	0.0228	0.04%	0.21%

The table 3.3 shows the calibration results determined as per the methodology in chapter 2 for probe with silica microsphere. The table also includes the average fluctuations for PSD sum and X diff signals. The Fig. 3.13 show the plots including PSD sum signal

variation as the reflected laser power changes (top), cantilever sensitivity for change in absorbed power (middle) and ambient temperature (bottom) respectively.
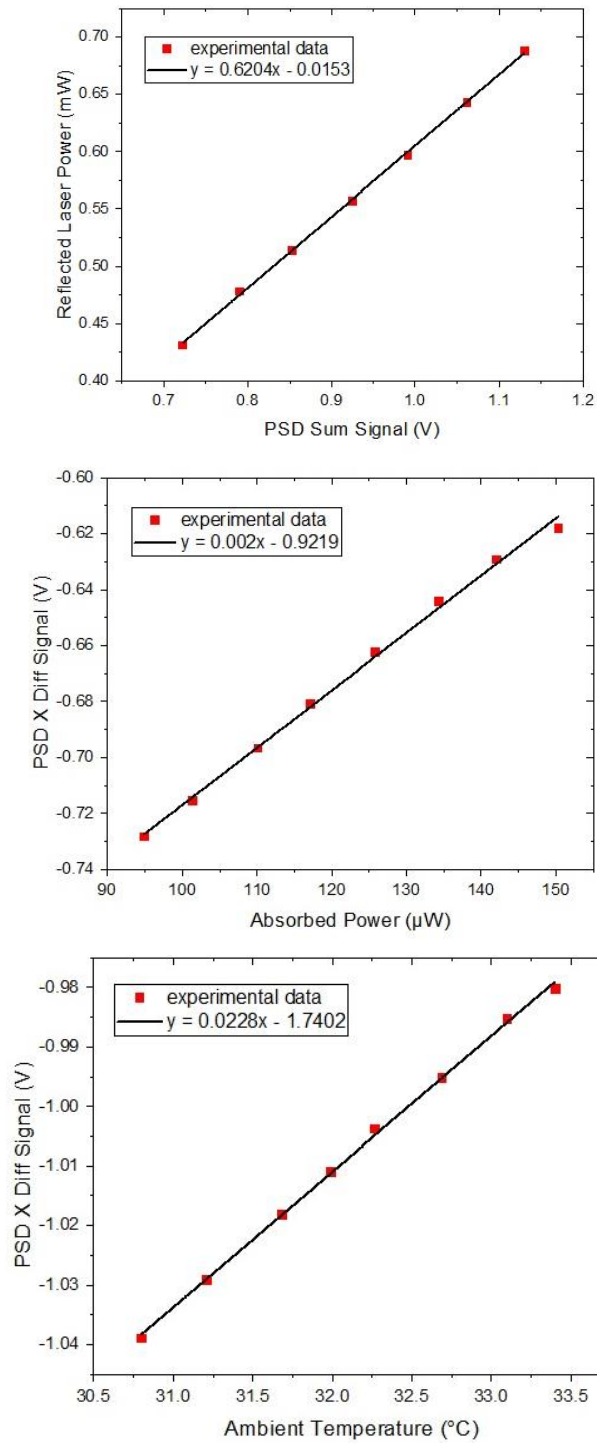
Figure 3.13: Calibration Plots for Probe with Silica Microsphere: (Top) Reflected Laser Power vs. PSD Sum Signal, (Middle) Cantilever Sensitivity vs. Absorbed Power, and (Bottom) Cantilever Sensitivity vs. Ambient Temperature.

37

The vacuum pressure is in the range of 9.72×10^{-2} Pa to 9.25×10^{-2} Pa during the calibration of AFM sensitivity with respect to change in absorbed power. The thermal conductance is 5.7 μW/°C according Eq. 2.11. Also, the tip temperature is calculated using Eq. 2.13 for various absorbed powers while the setup is under vacuum, as shown in Fig. 3.14. The ambient temperature inside the vacuum chamber is 24.5°C.
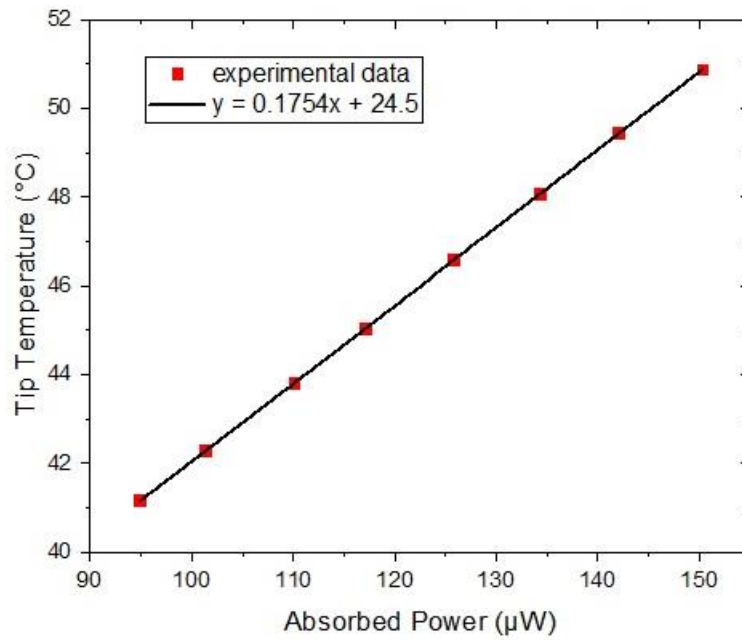
Figure 3.14: Tip Temperature vs. Absorbed Power in Vacuum for AFM Probe with Silica Microsphere

CHAPTER 4 NEAR-FIELD RADIATION MEASUREMENT BETWEEN SILICA

SPHERE AND GLASS PLATE

4.1 Experimental Procedures

All the required procedures to determine the near-field radiation heat conductance are depicted in the flow chart below.

```
┌─────────────────────────────────────────────────────────────┐
│      Attach the silica microsphere to the AFM cantilever tip   │
└─────────────────────────────────────────────────────────────┘
                              │
                              ▼
┌─────────────────────────────────────────────────────────────┐
│   Repeat the steps to determine the thermal conductance of the │
│                    cantilever with microsphere                 │
└─────────────────────────────────────────────────────────────┘
                              │
                              ▼
┌─────────────────────────────────────────────────────────────┐
│   Implement precise motion control to bring the sample in close │
│   distance with the silica microsphere from a few micrometers  │
│                  to a few tens of nanometers                   │
└─────────────────────────────────────────────────────────────┘
                              │
                              ▼
┌─────────────────────────────────────────────────────────────┐
│   Deduce the near-field radiation heat conductance through the │
│      PSD deflection signal change at different gap distances   │
└─────────────────────────────────────────────────────────────┘
                              │
                              ▼
┌─────────────────────────────────────────────────────────────┐
│   Process the data and plot heat transfer conductance and      │
│                      distance curve                            │
└─────────────────────────────────────────────────────────────┘
                              │
                              ▼
┌─────────────────────────────────────────────────────────────┐
│   Validate the experimental near-field radiation conductance   │
│                        with theory                             │
└─────────────────────────────────────────────────────────────┘
                              │
                              ▼
┌─────────────────────────────────────────────────────────────┐
│   Use the established near-field radiation heat transfer       │
│   metrology setup to plot the heat conductance and distance    │
│   curves for silica microsphere and silicon carbide substrate  │
└─────────────────────────────────────────────────────────────┘
```

The silica substrate is placed on a L-Bracket which is attached to the piezo motion control. Both the L-Bracket and piezo stage are attached to manual XY translation stages (Thorlabs, MT1) such that the distance between the substrate and the silica sphere can be reduced coarsely to approximately 10 μm with a differential adjuster (Thorlabs, DM10) at a resolution of 0.5 μm. The laser is kept ON and the PSD sum signal should be constant while the coarse approaching is performed to ensure the good alignment of AFM cantilever tip with laser beam not disturbed. Also, the lateral translation stage is used to move the substrate such that the reflected signal is not blocked by the substrate. Figure 4.1(a) shows the experimental setup with piezo motion control and translation stages.
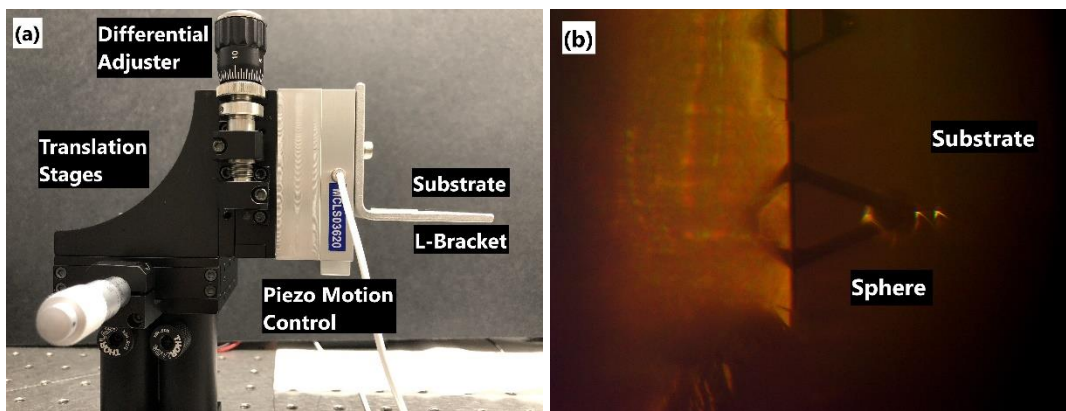
Figure 4.1: Optical Photos of (a) Experimental Setup with Piezo Motion Stage and Manual Translation Stages, and (b) Sphere and Substrate at Approximately 10 μm Gap

After the stage is moved close to the sphere manually, it is stopped after the gap reaches approximately 10 μm as shown in Fig. 4.1(b). The vacuum chamber is now closed with the cover plate and vacuum pump is turned on to pump the chamber down. Once the required vacuum pressure is achieved, the piezo motion stage is used to decrease the gap between substrate and sphere by 50 nm each time for which both PSD sum and difference signals are collected and averaged over 1000 data points. When the distance starts decreasing there is change in deflection of the cantilever which can be seen from the PSD

40

signals. The smallest or reference gap position of ~ 30 nm is determined when the substrate touches the sphere due to usual snap-in where there is a sudden and steep change in the PSD difference signal. Now the gap is slowly increased while collecting the PSD sum and difference signals at every step for 1000 points. Using Eqns. 2.16 and 2.17 the near-field conductance is calculated with the data measured at each step. From the determined G_{NFR} at every distance d the heat transfer conductance and distance curve is plotted.

4.2 Experimental Near-Field Conduction in Comparison with Theory

4.2.1 Near-Field Conductance Measurement

After the substrate is brought closer to the sphere manually using the translation stages, the piezo motion control stage zero position is checked using a multimeter provided with the Nano drive kit. Once the vacuum pressure reaches below 0.1 Pa the piezo is moved closer to the sphere in step sizes of 200 nm, 100 nm, 50 nm and 10 nm till there is a jump in PSD sum and X diff signal indicating the contact between microsphere and substrate.

Using the raw data collected, the PSD sum signal and X diff signal Vs position of the substrate is plotted as shown in Fig. 4.2. From the figure it can be seen that the slope of the curve is steep for both PSD sum and X diff signal at 9.4 μm making it the contact point.
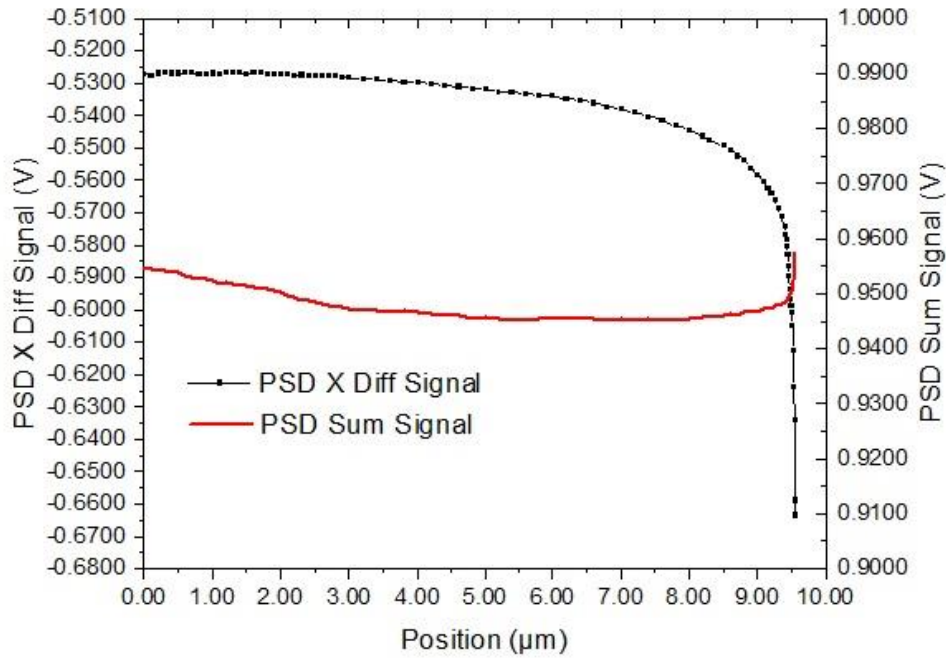
Figure 4.2: Plot of PSD Sum Signal and PSD X Difference Signal Vs. Position of Raw
Data for Probe with Silica Microsphere while the Substrate is Approaching

Using the Eqns. 2.13 and 2.14 the $T'_{sp}(10)$ and Q_{abs} are calculated. Also, from the

methodology used in chapter 2 and Eqns. 2.15, 2.16 and 2.17 the near-field conductance is

calculated at every d. The negative values of G_{NFR} from positions 0.2 µm to 2.1 µm is due

to PSD X Diff signal fluctuations in the initial approaching of substrate to the microsphere.

As the microsphere moved which is shown in Fig. 4.3 after the contact making it difficult

to determine at which position the exact contact point happened. The cantilever can bend

if there is a contact between the cantilever and substrate. This makes the PSD X diff signal

jump too. Now using the calculated near-field conductance values at every d, the plot

between near-field conductance and position of the substrate can be plotted as shown in

Fig. 4.4. Also, the initial values from 0.2 µm to 2.1 µm are not considered in the Fig. 4.4.
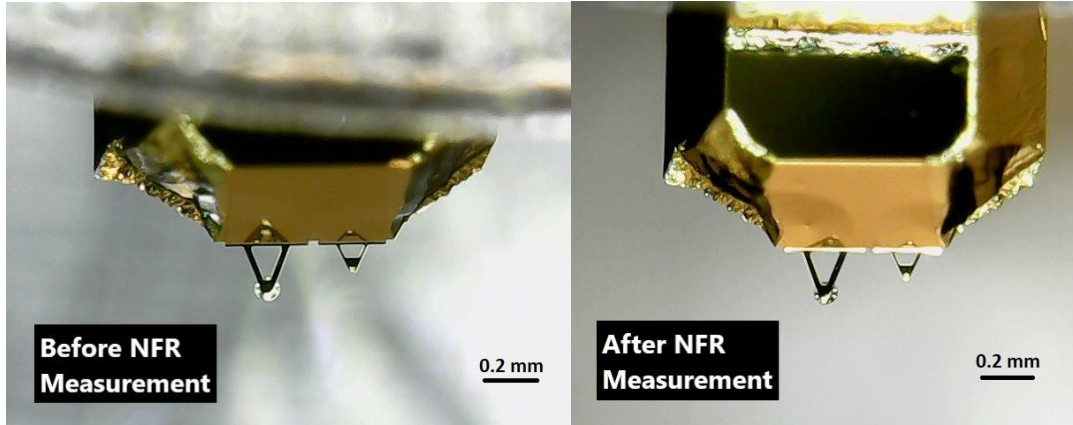
Figure 4.3: AFM Cantilever Probe with Silica Microsphere before NFR Measurement
(Left) and after NFR Measurement (Right)
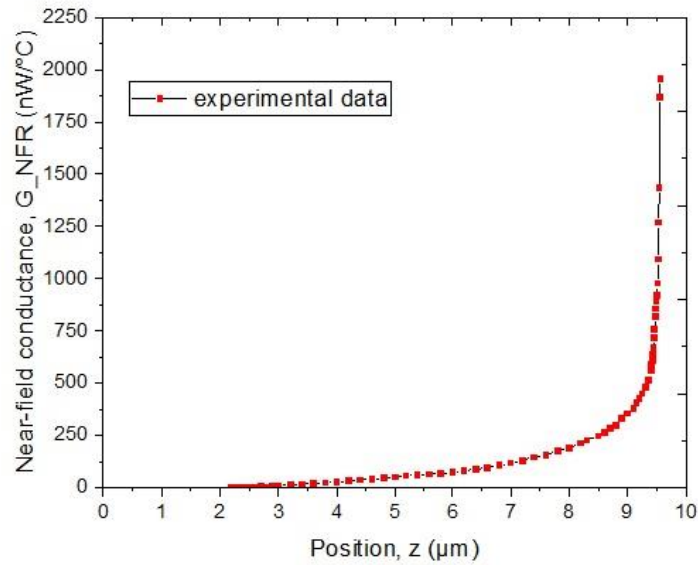
Figure 4.4: Plot between Near-Field Conductance and Position for Probe with Silica
Sphere as the Substrate is Approaching

Now that the contact position is considered to be at 9.4 μm, the gap d can be

determined using the relation $d = 9.4 - z$, where z is the position in μm. The calculated

gap d along with the near-field conductance are the plotted (heat transfer conductance

and distance curve) as shown in Fig 4.5.
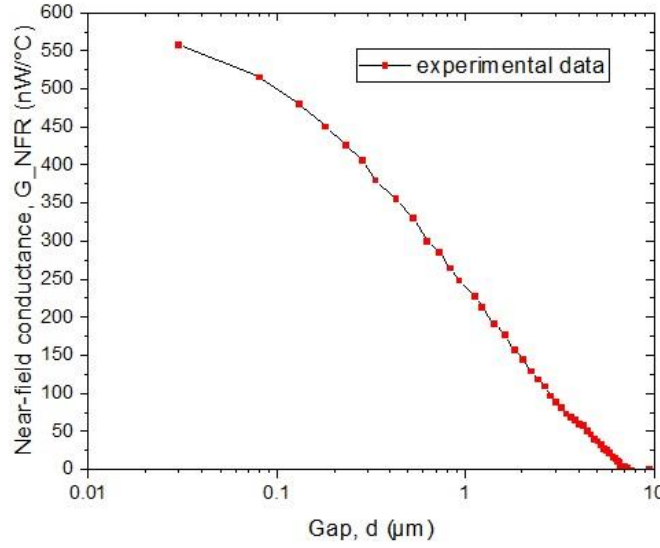
Figure 4.5: Plot between Near-Field Conductance and Gap for Probe with Silica Microsphere

From the results the near-field conductance value at the gap of 30 nm is 557 nW/°C. This value is for a 100 μm silica and silica substrate. Shen et al [2, 3] determined the near field conductance experimentally between 50 μm silica and silica substrate at 30 nm to be approximately 25 nW/°C.

The theoretical near-field conductance value for 100 μm silica microsphere can be calculated using the proximity approximation theory. The Eqn. 4.1. shows the near-field conductance between a sphere and plate using the heat transfer coefficient between two plates. As the only difference between 50 μm silica and 100 μm silica is the radius of the sphere, the calculated near-field conductance value for 100 μm silica will be approximately double the value of 50 μm silica (50 nW/°C).

$$G_{near-field}^{sphere-plate}(d) \cong 2\pi R \int_{s=d}^{d+R} h_{near-field}^{plate-plate}(s)ds \qquad (4.1)$$

where G is the near-field conductance, h is the heat transfer coefficient [38], R is the radius of the sphere and s is the step size.

Compared to Shen et al [2] the experimental near-field conductance value for probe with 100 μm silica microsphere is 10 times larger. One main cause for this drastic increase is due to the low sensitivity of cantilever with respect to change in ambient temperature and absorbed power. Therefore, further analysis is required in calibrating the thermal conductance of the bi-material cantilevers using the methodology mentioned in chapter 2.

CHAPTER 5 CONCLUSIONS AND FUTURE WORK

The setup for the novel thermal metrology based on AFM bi-material cantilever to experimentally measure near-field thermal radiation is finished. The LABVIEW software is used to collect the data points during the experiment. The transmittance of the optics of the setup is determined. Using the setup, the different AFM bi-material cantilevers thermal conductance is calibrated to help find the near-field radiation between the silica sphere and silica substrate. Finally, the substrate is brought closer to the microsphere using the piezo motion control and near-field conductance is calculated at every gap d.

The near-field conductance vs. *d* plot is analyzed and the exact contact point is determined and compared it with theoretical calculations. The experimentally calculated near-field conductance values are compared to theoretical calculations using the proximity approximation theorem for a silica microsphere of 100 μm diameter and silica substrate and compared the results with Shen et al [2, 3]. As compared to Shen et al [2] the near-field conductance values are 10 times larger which requires further analysis.

The main cause for the higher conductance values is due to low sensitivity of cantilever with respect to change in ambient temperature and absorbed power. The sensitivity due to change in ambient temperature can be improved by implementing more stable heating method of the cantilever, using more sensitive PSD.

Stronger signals with less fluctuation data can be obtained for the near-field radiation by increasing the tip temperature of the AFM cantilever. The tip temperature depends on three parameters. The absorptance of the cantilever, incident laser power and the thermal conductance of the cantilever. To improve the absorptance, the tip can be coated with nickel to increase the absorptance. As the new layer of coating changes the

AFM sensitivity, all the calibration needs to be repeated for further analysis. Also, to increase the tip temperature the G value needs to decrease. A new AFM cantilever with Pyrex base (NanoAndMore, PNP-TR-TL) will be used.

After the setup is validated with Shen et al [2, 3] new near-field radiation heat transfer measurements are measured between silica microsphere and SiC plate, SiC metasurfaces using the novel metrology.

REFERENCES

1. Michael F. Modest (2013). Radiative Heat Transfer, Third Edition.

2. Sheng Shen, Arvind Narayanaswamy, Gang Chen. (2009). Surface Phonon Polaritons Mediated Energy Transfer between Nanoscale Gaps. Nano Letters, 9, 8, 2909-2913.

3. Arvind Narayanaswamy, Sheng Shen, and Gang Chen. (2008). Near-field radiative heat transfer between a sphere and a substrate. Physical Review, B 78, 115303.

4. Basu, S., Chen, Y.B., and Zhang, Z.M. (2007). Microscale Radiation in Thermophotovoltaic Devices - a Review. International Journal of Energy Research, 31(6-7), 689–716.

5. De Wilde, Y., Formanek, F., Carminati, R., Gralak, B., Lemoine, P.A., Joulain, K., Mulet, J.P., Chen, Y., and Greffet, J.J. (2006). Thermal Radiation Scanning Tunnelling Microscopy. Nature, 444(7120), 740–743.

6. Kittel, A., Muller-Hirsch, W., Parisi, J., Biehs, S.A., Reddig, D., and Holthaus, M. (2005). Near-Field Heat Transfer in a Scanning Thermal Microscope. Physical Review Letters, 95(22), 224301.

7. Otey, C.R., Lau,W.T., and Fan, S. (2010). Thermal Rectification Through Vacuum. Physical Review Letters, 104(15), 154301.

8. Basu, S., and Francoeur, M. (2011a). Near-Field Radiative Transfer Based Thermal Rectification Using Doped Silicon. Applied Physics Letters, 98(11), 113106.

9. Liu, Z.W., Wei, Q.H., and Zhang, X. (2005). Surface Plasmon Interference Nanolithography. Nano Letters, 5(5), 957–961.

10. Wang, L., Uppuluri, S.M., Jin, E.X., and Xu, X. (2006). Nanolithography Using High Transmission Nanoscale Bowtie Apertures. Nano Letters, 6(3), 361–364.

11. M. Planck. (1991). The Theory of Heat Radiation Dover, New York.

12. S. M. Rytov. (Air Force Cambridge Research Center, Bedford, MA, 1959). Theory of Electric Fluctuations and Thermal Radiation.

13. D. Polder and M. Van Hove. (1971). Theory of radiative heat transfer between closely spaced bodies. Physical Review, B 4, 3303.

14. G. A. Domoto, R. F. Boehm, C. L. Tien. (1970). Experimental Investigation of Radiative Transfer Between Metallic Surfaces at Cryogenic Temperatures. Journal of Heat Transfer, 92(3), 412-416.

15. C. M. Hargreaves. (1973). Philips Research Reports, Suppl. 5, 1.

16. J. B. Xu, K. Lauger, R. Moller, K. Dransfeld, and I. H. Wilson. (1994). Journal of Applied Physics 76, 7209.

17. Arvind Narayanaswamy, Sheng Shen, Lu Hu, Xiaoyuan Chen, Gang Chen. (2009). Breakdown of the Planck blackbody radiation law at nanoscale gaps. Applied Physics A, Volume 96, Issue 2, pp 357–362.

18. A. Narayanaswamy, G. Chen, in Annual Review of Heat Transfer, vol. 14, ed. by V. Prasad, Y. Jaluria, G. Chen (Begell House, Reading, 2005), p. 169.

19. J. Weber. (1956). Fluctuation Dissipation Theorem. Physical Review, 101, 1620.

20. Herbert B. Callen and Theodore A. Welton. (1951). Irreversibility and Generalized Noise. Physical Review, 83, 34.

21. L.D. Landau, E.M. Lifshitz, Statistical Physics (Addison-Wesley, Reading, 1969).

22. Jesse I. Watjen, Bo Zhao, and Zhuomin M. Zhang. (2016). Near-field radiative heat transfer between doped-Si parallel plates separated by a spacing down to 200 nm. Applied Physics Letters, 109, 203112.

23. A. Kittel, W. Muller-Hirsch, J. Parisi, S. Biehs, D. Reddig, and M. Holthaus. (2005). Near-Field Heat Transfer in a Scanning Thermal Microscope. Physical Review Letters, 95, 224301.

24. Kyeongtae Kim, Bai Song, Víctor Fernández-Hurtado, Woochul Lee, Wonho Jeong, Longji Cui, Dakotah Thompson, Johannes Feist, M. T. Homer Reid, Francisco J. García-Vidal, Juan Carlos Cuevas, Edgar Meyhofer1 & Pramod Reddy. (2015). Radiative heat transfer in the extreme near field. Nature, Vol. 528, Issue. 7582, 387-391.

25. Longji Cui, Wonho Jeong, Víctor Fernández-Hurtado, Johannes Feist, Francisco J. García-Vidal, Juan Carlos Cuevas, Edgar Meyhofer and Pramod Reddy. (2017). Study of radiative heat transfer in Ångström- and nanometre-sized gaps. Nature Communications volume 8, 14479.

26. J. R. Barnes, R. J. Stephenson, C. N. Woodburn, S. J. O. Shea, M. E. Welland, T. Rayment, J. K. Gimzewski, and Ch. Gerber. (1994). A femtojoule calorimeter using micromechanical sensors. Review of Scientific Instruments, 65, 3793.

27. J. K. Gimzewski, Ch. Gerber, E. Meyer, and R. R. Schlittler. (1994). Observation of a chemical reaction using a micromechanical sensor. Chemical Physical Letters, 217, 589.

28. J. Varesi, J. Lai, T. Perazzo, Z. Shi, A. Majumdar. (1997). Photothermal measurements at picowatt resolution using uncooled micro-optomechanical sensors. Applied Physics Letters, 71, 306.

29. P. G. Datskos, N. V. Lavrik, S. Rajic. (2004). Performance of uncooled microcantilever thermal detectors. Review of Scientific Instruments 75, 1134.

30. Beomjin Kwon, Matthew Rosenberger, Rohit Bhargava, David G. Cahill, and William P. King. (2012). Dynamic thermomechanical response of bimaterial

microcantilevers to periodic heating by infrared radiation. Review of Scientific Instruments 83, 015003.

31. Arvind Narayanaswamy and Gang Chen. (2008). Thermal near-field radiative transfer between two spheres. Physical Review, B 77, 075125.

32. C. F. Bohren and D. R. Huffman. (1983). Absorption and Scattering of Light by Small Particles, Wiley, New York.

33. Sheng Shen, Arvind Narayanaswamy, Shireen Goh, Gang Chen. (2008). Thermal conductance of bi-material microcantilevers. Applied Physics Letters, 92, 063509.

34. R. J. Roark and W. C. Young. (1975). Formulas for Stress and Strain, 5th ed. McGraw-Hill, New York.

35. J.Lai, T.Perazzo, Z.Shi, A.Majumdar. Optimization and performance of high-resolution micro-optomechanical thermal sensors. Sensors and Actuators A: Physical Volume 58, Issue 2, Pages 113-119.

36. A. F. Mills, Heat Transfer, 2nd ed. (Prentice-Hall, Engleweed Cliffs, NJ, 1999).

37. Kota Ito, Atsushi Miura, Hideo Iizuka, and Hiroshi Toshiyoshi. (2015). Parallel-plate submicron gap formed by micromachined low-density pillars for near-field radiative heat transfer. Applied Physics Letters, 106, 083504.

38. S. Basu, Z. M. Zhang and C. J. Fu. (2009). Review of near-field thermal radiation and its application to energy conversion. International Journal of Energy Research, 33, 1203–1232.

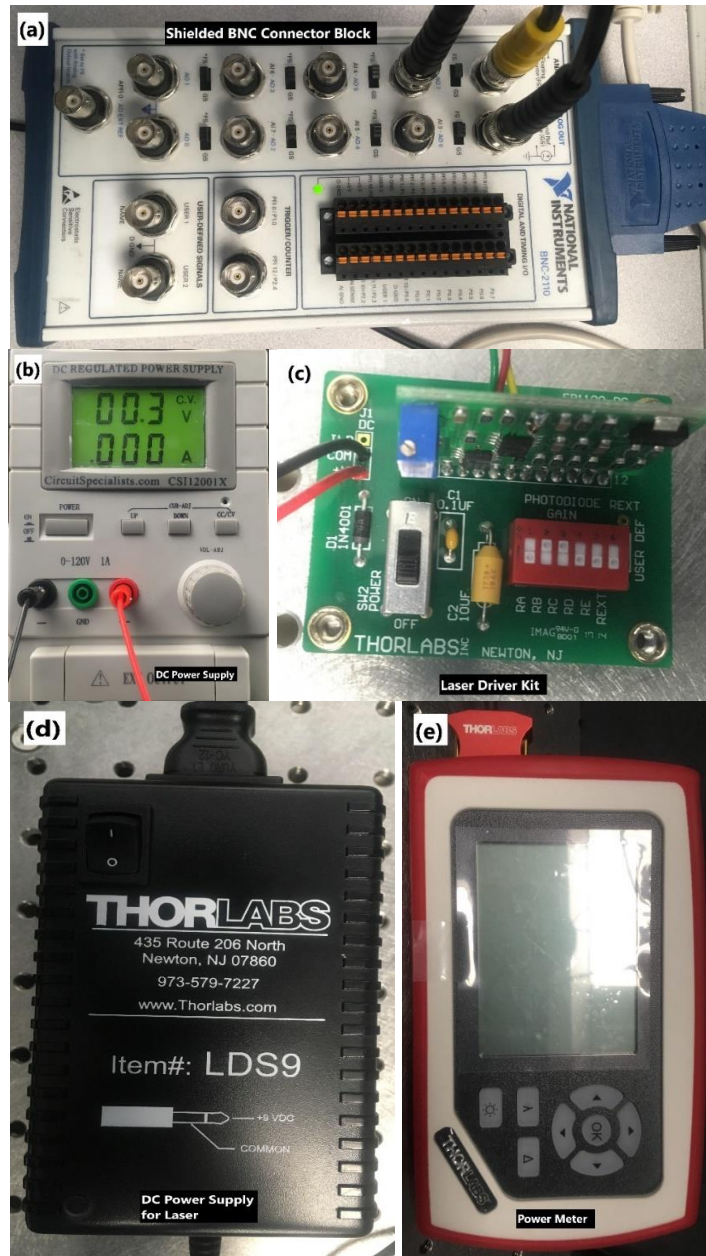APPENDIX A

MAJOR PARTS USED IN THE EXPERIMENTAL SETUP

Figure 1: (a)Shielded BNC Connector Block; (b)DC Power Supply;
(c)Laser Driver Kit; (d)DC Power Supply for Laser; (e)Power Meter

Figure 2: Position Sensing Amplifier

APPENDIX B

RAW DATA COLLECTED DURING THE EXPERIMENT

Table 1.1: Raw Data Collected Including Fluctuations During the Substrate Approaching the Microsphere in Vacuum

Pressure (Pa)	Position (μm)	PSD Diff. X (V)			PSD Sum (V)		
		Avg	std	fluctuation	Avg	std	fluctuation
0.0953	0	-0.5272	0.0020	-0.375%	0.9549	0.0003	0.030%
0.0944	0.1	-0.5274	0.0019	-0.356%	0.9545	0.0003	0.031%
0.0944	0.2	-0.5268	0.0019	-0.366%	0.9543	0.0003	0.031%
0.0943	0.3	-0.5267	0.0020	-0.371%	0.9541	0.0003	0.030%
0.0940	0.4	-0.5268	0.0019	-0.355%	0.9539	0.0003	0.034%
0.0937	0.5	-0.5268	0.0019	-0.368%	0.9539	0.0003	0.030%
0.0934	0.6	-0.5267	0.0019	-0.364%	0.9534	0.0003	0.029%
0.0931	0.7	-0.5267	0.0020	-0.371%	0.9530	0.0003	0.031%
0.0930	0.8	-0.5270	0.0020	-0.374%	0.9527	0.0003	0.032%
0.0929	0.9	-0.5269	0.0019	-0.362%	0.9528	0.0003	0.031%
0.0927	1	-0.5269	0.0020	-0.374%	0.9524	0.0003	0.030%
0.0927	1.1	-0.5269	0.0019	-0.369%	0.9517	0.0003	0.032%
0.0924	1.2	-0.5268	0.0019	-0.359%	0.9520	0.0003	0.031%
0.0923	1.3	-0.5267	0.0020	-0.372%	0.9518	0.0003	0.032%
0.0922	1.4	-0.5267	0.0019	-0.369%	0.9515	0.0003	0.031%
0.0920	1.5	-0.5269	0.0019	-0.368%	0.9513	0.0003	0.031%
0.0918	1.6	-0.5267	0.0019	-0.362%	0.9513	0.0003	0.029%
0.0917	1.7	-0.5266	0.0019	-0.354%	0.9510	0.0003	0.031%
0.0915	1.8	-0.5271	0.0019	-0.367%	0.9509	0.0003	0.035%
0.0913	1.9	-0.5269	0.0018	-0.337%	0.9504	0.0003	0.027%
0.0911	2	-0.5271	0.0019	-0.356%	0.9502	0.0003	0.028%
0.0906	2.1	-0.5271	0.0019	-0.354%	0.9498	0.0003	0.033%
0.0905	2.2	-0.5275	0.0018	-0.346%	0.9493	0.0003	0.032%
0.0902	2.3	-0.5273	0.0018	-0.348%	0.9489	0.0003	0.029%
0.0902	2.4	-0.5274	0.0020	-0.374%	0.9486	0.0003	0.030%
0.0899	2.5	-0.5277	0.0019	-0.366%	0.9483	0.0003	0.035%
0.0897	2.6	-0.5276	0.0018	-0.350%	0.9483	0.0003	0.032%
0.0895	2.7	-0.5277	0.0020	-0.379%	0.9479	0.0003	0.032%
0.0895	2.8	-0.5277	0.0020	-0.373%	0.9476	0.0003	0.032%
0.0892	2.9	-0.5282	0.0020	-0.373%	0.9474	0.0003	0.028%
0.0889	3	-0.5282	0.0020	-0.369%	0.9471	0.0003	0.032%
0.0887	3.2	-0.5286	0.0019	-0.363%	0.9470	0.0003	0.031%
0.0887	3.4	-0.5288	0.0019	-0.361%	0.9471	0.0003	0.029%
0.0886	3.6	-0.5292	0.0020	-0.376%	0.9468	0.0003	0.030%

		PSD Diff. X (V)			PSD Sum (V)		
Pressure (Pa)	Position (μm)	Avg	std	fluctuation	Avg	std	fluctuation
0.0884	3.8	-0.5295	0.0020	-0.375%	0.9470	0.0003	0.031%
0.0882	4	-0.5297	0.0019	-0.368%	0.9466	0.0003	0.033%
0.0880	4.2	-0.5302	0.0019	-0.366%	0.9462	0.0004	0.037%
0.0880	4.4	-0.5306	0.0019	-0.357%	0.9459	0.0003	0.031%
0.0876	4.6	-0.5309	0.0020	-0.372%	0.9460	0.0003	0.033%
0.0876	4.8	-0.5315	0.0020	-0.369%	0.9456	0.0003	0.032%
0.0875	5	-0.5319	0.0020	-0.379%	0.9456	0.0003	0.029%
0.0868	5.2	-0.5325	0.0019	-0.358%	0.9454	0.0003	0.032%
0.0866	5.4	-0.5327	0.0019	-0.360%	0.9452	0.0003	0.032%
0.0865	5.6	-0.5331	0.0019	-0.362%	0.9452	0.0003	0.030%
0.0864	5.8	-0.5335	0.0019	-0.355%	0.9455	0.0003	0.030%
0.0862	6	-0.5339	0.0019	-0.365%	0.9455	0.0003	0.031%
0.0860	6.2	-0.5346	0.0018	-0.345%	0.9455	0.0003	0.028%
0.0858	6.4	-0.5353	0.0018	-0.344%	0.9456	0.0003	0.032%
0.0858	6.6	-0.5360	0.0018	-0.331%	0.9453	0.0003	0.027%
0.0855	6.8	-0.5371	0.0018	-0.340%	0.9452	0.0003	0.033%
0.0857	7	-0.5379	0.0019	-0.355%	0.9453	0.0003	0.033%
0.0852	7.2	-0.5389	0.0018	-0.328%	0.9453	0.0003	0.029%
0.0852	7.4	-0.5403	0.0019	-0.344%	0.9454	0.0003	0.029%
0.0852	7.6	-0.5413	0.0019	-0.356%	0.9453	0.0003	0.028%
0.0849	7.8	-0.5431	0.0020	-0.360%	0.9453	0.0003	0.028%
0.0850	8	-0.5443	0.0019	-0.355%	0.9455	0.0003	0.029%
0.0850	8.2	-0.5463	0.0020	-0.357%	0.9457	0.0003	0.033%
0.0849	8.3	-0.5475	0.0019	-0.352%	0.9457	0.0003	0.030%
0.0845	8.5	-0.5493	0.0020	-0.361%	0.9459	0.0003	0.030%
0.0845	8.6	-0.5506	0.0019	-0.346%	0.9463	0.0003	0.033%
0.0843	8.7	-0.5524	0.0018	-0.326%	0.9461	0.0003	0.029%
0.0842	8.8	-0.5536	0.0019	-0.351%	0.9467	0.0003	0.030%
0.0836	8.9	-0.5561	0.0019	-0.342%	0.9467	0.0003	0.031%
0.0834	9	-0.5582	0.0019	-0.347%	0.9467	0.0003	0.030%
0.0834	9.1	-0.5602	0.0020	-0.348%	0.9471	0.0003	0.030%
0.0831	9.15	-0.5623	0.0020	-0.349%	0.9473	0.0003	0.031%
0.0831	9.2	-0.5640	0.0019	-0.341%	0.9473	0.0003	0.035%
0.0829	9.25	-0.5659	0.0020	-0.350%	0.9477	0.0003	0.031%
0.0828	9.3	-0.5683	0.0020	-0.352%	0.9478	0.0003	0.030%
0.0826	9.35	-0.5710	0.0019	-0.332%	0.9480	0.0002	0.025%
0.0826	9.4	-0.5743	0.0020	-0.348%	0.9484	0.0003	0.036%

Pressure (Pa)	Position (μm)	PSD Diff. X (V)			PSD Sum (V)		
		Avg	std	fluctuation	Avg	std	fluctuation
0.0824	9.41	-0.5767	0.0019	-0.330%	0.9486	0.0003	0.033%
0.0820	9.42	-0.5784	0.0019	-0.335%	0.9488	0.0003	0.031%
0.0816	9.43	-0.5803	0.0020	-0.340%	0.9487	0.0003	0.030%
0.0817	9.44	-0.5829	0.0019	-0.320%	0.9487	0.0003	0.031%
0.0814	9.45	-0.5864	0.0018	-0.314%	0.9489	0.0003	0.029%
0.0811	9.46	-0.5893	0.0018	-0.309%	0.9494	0.0003	0.034%
0.0811	9.47	-0.5936	0.0019	-0.313%	0.9494	0.0003	0.029%
0.0806	9.48	-0.5965	0.0019	-0.319%	0.9499	0.0003	0.027%
0.0805	9.49	-0.5988	0.0018	-0.307%	0.9502	0.0003	0.030%
0.0803	9.5	-0.6008	0.0020	-0.327%	0.9506	0.0003	0.032%
0.0793	9.51	-0.6049	0.0020	-0.326%	0.9506	0.0003	0.029%
0.0792	9.52	-0.6125	0.0019	-0.314%	0.9510	0.0003	0.029%
0.0791	9.53	-0.6238	0.0020	-0.328%	0.9523	0.0003	0.032%
0.0789	9.54	-0.6342	0.0020	-0.315%	0.9535	0.0003	0.032%
0.0787	9.55	-0.6587	0.0019	-0.293%	0.9568	0.0003	0.031%
0.0782	9.56	-0.6636	0.0020	-0.302%	0.9572	0.0003	0.032%

Table 1.2: Calculated Near-Field Conductance Data at Every Position

Position (μm)	G_NFR (nW/°C)	Position (μm)	G_NFR (nW/°C)	Position (μm)	G_NFR (nW/°C)
0	0.000	3.6	21.505	9.2	426.598
0.1	1.166	3.8	24.745	9.25	450.391
0.2	-4.609	4	26.921	9.3	480.865
0.3	-5.926	4.2	32.019	9.35	515.408
0.4	-4.848	4.4	36.775	9.4	557.477
0.5	-4.273	4.6	39.933	9.41	588.029
0.6	-6.046	4.8	46.112	9.42	611.172
0.7	-5.317	5	50.314	9.43	635.568
0.8	-2.870	5.2	57.463	9.44	670.631
0.9	-4.076	5.4	59.882	9.45	717.707
1	-4.169	5.6	64.527	9.46	758.062
1.1	-3.143	5.8	68.786	9.47	818.535
1.2	-5.263	6	73.192	9.48	857.828
1.3	-5.544	6.2	81.002	9.49	891.553
1.4	-5.779	6.4	88.694	9.5	920.103
1.5	-3.339	6.6	96.509	9.51	979.380
1.6	-6.244	6.8	109.163	9.52	1093.162
1.7	-6.485	7	117.938	9.53	1268.852
1.8	-1.227	7.2	129.033	9.54	1436.872
1.9	-3.610	7.4	145.052	9.55	1867.159
2	-2.057	7.6	156.710	9.56	1958.674
2.1	-1.105	7.8	176.762		
2.2	2.680	8	191.267		
2.3	0.265	8.2	213.403		
2.4	2.149	8.3	227.579		
2.5	4.606	8.5	248.597		
2.6	3.731	8.6	264.358		
2.7	4.822	8.7	285.765		
2.8	4.651	8.8	299.680		
2.9	10.055	8.9	329.952		
3	10.477	9	355.388		
3.2	14.670	9.1	380.095		
3.4	16.423	9.15	406.193		